Title
Characterization of Superconductivity in Compressively Strained SrTiO3 Thin Films

Author
Jeong, Hanbyeol

Publication Date
2022

Peer reviewed|Thesis/dissertation

UNIVERSITY OF CALIFORNIA

Santa Barbara

Characterization of Superconductivity in Compressively Strained $SrTiO_3$ Thin Films

A dissertation submitted in partial satisfaction of the

requirements for the degree

Doctor of Philosophy

in

Materials

by

Hanbyeol Jeong

Committee in charge:

Professor Susanne Stemmer, Chair

Professor John Harter

Professor Stephen Wilson

Professor Andrea Young

September 2022

The dissertation of Hanbyeol Jeong is approved.

_____

Professor John Harter

_____

Professor Stephen Wilson

_____

Professor Andrea Young

_____

Professor Susanne Stemmer, Committee Chair

August 2022

ACKNOWLEDGEMENTS

It has been my privilege to study in the doctoral program at UC Santa Barbara for four years. I thank my advisor Prof. Susanne Stemmer for granting me the opportunity to research oxide thin films and for consistently leading me in the right research directions. Above all, she encouraged me to keep motivated in research to complete the doctoral program.

I appreciate the highly collaborative atmosphere at UCSB. I would have never been able to make research progress without the support of my colleagues. I greatly thank our oxide project members, Nick Combs and Wangzhou Wu. We have had very fruitful experiences working together and having many discussions during my entire PhD study. I thank Timo Schumann, Kaveh Ahadi, Luca Galetti, Omor Shoron, and Billy Strickland who taught me MBE growth and electrical measurement at the start of my PhD. I also thank Salva Salmani-Rezaie and Tyler Pardue for their quality TEM images. Their work provided useful information which contributed to my research. I would like to thank Arman Rashidi and Robert Kealhofer for their skilled electrical measurement during the latter part of my PhD. I thank Simon Munyan and Jacob Brady for their elaboration on proofreading of my dissetation. I am very impressed with their detailed corrections comments. I am grateful to the rest of the Stemmer group members and alumni who made good memories with me: David Kealhofer, Alex Lygo, Evan Guo, Manic Goyal, Chris Freeze, Patrick Marshall, Raj Chaklashiya, and Biswajit Datta.

People outside the Stemmer group have supported me a lot as well. I thank Ryan Russell and Prof. John Harter for providing helpful optical measurements. I also would like to thank

the UCSB staff: Kurt Olsson, John English, Amanda Strom, Youli Li, and the UCSB nanofab engineers for their great efforts in the maintenance and improvement of their facilities.

Lastly, I am thankful for my family. They have always cheered my life while studying abroad in the U.S. I truly appreciate my wife, Seonghyeon. She made a hard decision to come to the U.S. in 2020 during the COVID lockdown period. She helped me endure the isolation at the time and continues to bring joy into my life.

Curriculum Vitae

Hanbyeol Jeong

EDUCATION

2018.09 – 2022.08	Doctor of Philosophy in Materials, University of California, Santa Barbara, United States
2012.09 – 2015.02	Master of Science in Materials Science & Engineering, Seoul National University, South Korea
2009.03 – 2012.02	Bachelor of Science in Materials Science & Engineering, Pohang University of Science and Technology, South Korea

PROFESSIONAL EMPLOYMENT

2020.01 – 2020.03	Teaching Assistant, Materials Department, University of California, Santa Barbara, United States
2015.01 – 2018.07	Device Engineer, Spin-Transfer-Torque MRAM Device Team, SK Hynix, South Korea

PUBLICATIONS

2022 **H. Jeong**, R. Russell, N. Combs, T. Pardue, J. Harter, S. Stemmer, Similarity in the critical thicknesses for superconductivity and ferroelectricity in strained $SrTiO_3$ films, *Appl. Phys. Lett.* **121**, 012601, 2022 [DOI]

2021 **H. Jeong**, N. Combs, S. Munyan. A. Rashidi, and S. Stemmer, Reducing surface depletion of superconducting $SrTiO_3$ films with $EuTiO_3$ capping layers, *Appl. Phys. Lett.* **119**, 162601, 2021 [DOI]

2021 S. Salmani-Rezaie, **H. Jeong**, R. Russell, J. W. Harter, and S. Stemmer, Role of locally polar regions in the superconductivity of $SrTiO_3$, *Phys. Rev. Mater.* **5**, 104801, 2021 [DOI]

2021 S. Salmani-Rezaie, L Galletti, T. Schumann, R. Russell, **H. Jeong**, Y. Li, J. W. Harter, and S. Stemmer, Superconductivity in magnetically doped $SrTiO_3$, *Appl. Phys. Lett.* **118**, 202602, 2021 [DOI]

2020 T. Schumann, L. Galletti, **H. Jeong**, K. Ahadi, W. M. Strickland, S. Salmani-Rezaie, and S. Stemmer, Possible signatures of mixed-parity superconductivity in doped polar $SrTiO_3$ films, *Phys. Rev. B*, **101**, 100503(R), 2020 [DOI]

2015 D. Han, Y. Cho, **H. Jeong**, and S. Kim, Perpendicular-bias-field control of coupled vortex oscillations in nanodot networks, *J. Appl. Phys.*, **117**, 083910, 2015, [DOI]

2014 **H. Jeong**, and S. Kim, Enhanced gyration-signal propagation speed in one-dimensional vortex-antivortex lattices and its control by perpendicular bias field, *Appl. Phys. Lett.* **105**, 222410, 2014, [DOI]

2013 D. Han, **H. Jeong**, S. Kim, Contrasting vortex-gyration dispersions for different lattice bases in one-dimensional vortex arrays, *Appl. Phys. Lett.*, 103, 112406, 2013, [DOI]

HONORS

Kwanjeong Educational Foundation Scholarship for Graduate Studies, 2018

Merit-based scholarship, Seoul National University, 2013

National Science & Technology Scholarship, Korea Student Aid Foundation, 2009

ABSTRACT

Characterization of Superconductivity in Compressively Strained $SrTiO_3$ Thin Films

by

Hanbyeol Jeong

Although superconductivity in strontium titanate ($SrTiO_3$) was discovered in the 1960s, the origin of superconductivity in $SrTiO_3$ has not been completely understood. Moreover, its unusual superconducting characteristics have made $SrTiO_3$ a fascinating playground to potentially study multiple aspects of unconventional superconductivity. For example, $SrTiO_3$ is one of the most dilute superconductors where standard Bardeen-Cooper-Schrieffer (BCS theory) is believed to be no longer valid. Furthermore, the presence of superconductivity and ferroelectricity and their interplay possibly leads to an unconventional pairing mechanism in $SrTiO_3$.

In this dissertation, high-quality, doped, ferroelectric, compressively strained $SrTiO_3$ thin films were grown using hybrid molecular beam epitaxy (MBE) to unveil unique superconducting properties. First, we present unconventional characteristics of relatively thick (160-180 nm) strained $SrTiO_3$ films. In some strained films, we show signatures of unusual superconducting states such as in-plane critical fields far above the Pauli limiting field and second harmonic resistances.

The study of superconductivity in ultra-thin $SrTiO_3$ films is hindered by strong surface carrier depletion, which makes thin films insulating. We solve this issue by introducing thin (~10 nm) $EuTiO_3$ capping layers. We show that the $EuTiO_3$ capping layer effectively prevents

strong carrier depletion in $SrTiO_3$ films and that a capped 40 nm-thick $SrTiO_3$ film becomes superconducting.

We utilize the $EuTiO_3$ capping layer to elucidate the connection between superconductivity and ferroelectricity in $SrTiO_3$ films. Systematic film thickness study shows that superconductivity and ferroelectricity are suppressed simultaneously in the $SrTiO_3$ films of thicknesses less than 40 nm. We speculate that this result implies that broken inversion symmetry (spin-orbit coupling) plays an important role in the superconductivity of strained $SrTiO_3$ films.

TABLE OF CONTENTS

Chapter 6. Summary and Future Directions

Chapter 1

Introduction and Background

1.1 Perovskite Oxides and $SrTiO_3$

Perovskite, which is originally the mineral name of calcium titanate ($CaTiO_3$), describes a crystal structure adopted by compounds with the chemical formula ABX_3. The elements A and B are cations, and X is an anion. Therefore, X is fixed to oxygen for perovskite oxides. Figure 1.1 illustrates the crystal structure of a perovskite oxide. A-sites are located at the vertices of a unit cell. B-sites and oxygen-sites are body-centered and face-centered, respectively. Generally, alkaline- or rare-earth elements occupy A-sites, and transition metal elements occupy B-sites [1]. The high degree of freedom of chemical composition makes perovskite oxides an attractive platform.

Strontium titanate ($SrTiO_3$) is a representative perovskite oxide, and it has been widely used as a substrate for complex oxide growth. Moreover, $SrTiO_3$ itself exhibits rich physics with high tunability, which has motivated researchers over several decades. This dissertation deals with superconductivity of $SrTiO_3$ thin films. Although superconductivity in $SrTiO_3$ was first discovered in the 1960s [2,3], its nature is still not fully understood. For example, its pairing mechanism has been the source of long-standing debate [4]. This chapter introduces the basic physical properties of $SrTiO_3$ which are related to understanding the superconductivity in $SrTiO_3$. More information about $SrTiO_3$ is comprehensively discussed in recent review papers [5,6].

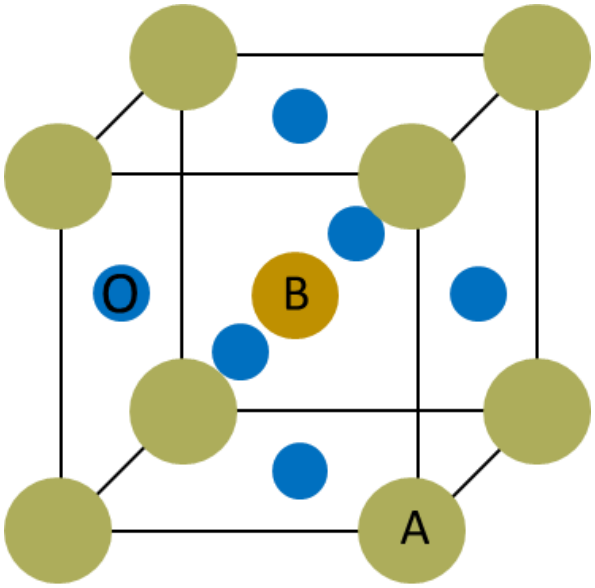

Figure 1.1. Crystal structure of a perovskite oxide (ABO_3). B-sites and oxygen-sites are body-centered and face-centered, respectively.

1.2 Crystal structure and structural transition of $SrTiO_3$

At room temperature, $SrTiO_3$ has a cubic perovskite crystal structure with a lattice parameter of 3.905 Å. This value is intermediate in the lattice parameters of perovskite oxides [7], which is why $SrTiO_3$ is a common substrate for oxide film growth. As shown in Figure 1.2a, the face-centered six oxygen atoms form an octahedron. At 105 K, $SrTiO_3$ undergoes a structural transition from cubic to tetragonal along with a rotation of the oxygen octahedron (antiferrodistortive transition) [8–10]. The rotation axis can be along the a, b, or c axis. This degree of freedom gives rise to the formation of domains with respect to the rotation axis [8]. Further structural transitions to orthorhombic (65 K) and possibly rhombohedral (10 K) were reported using x-ray diffraction [8]. Meanwhile, external perturbations can lead to a ferroelectric transition accompanied by inversion symmetry breaking. The details of ferroelectricity in $SrTiO_3$ will be discussed in this chapter.

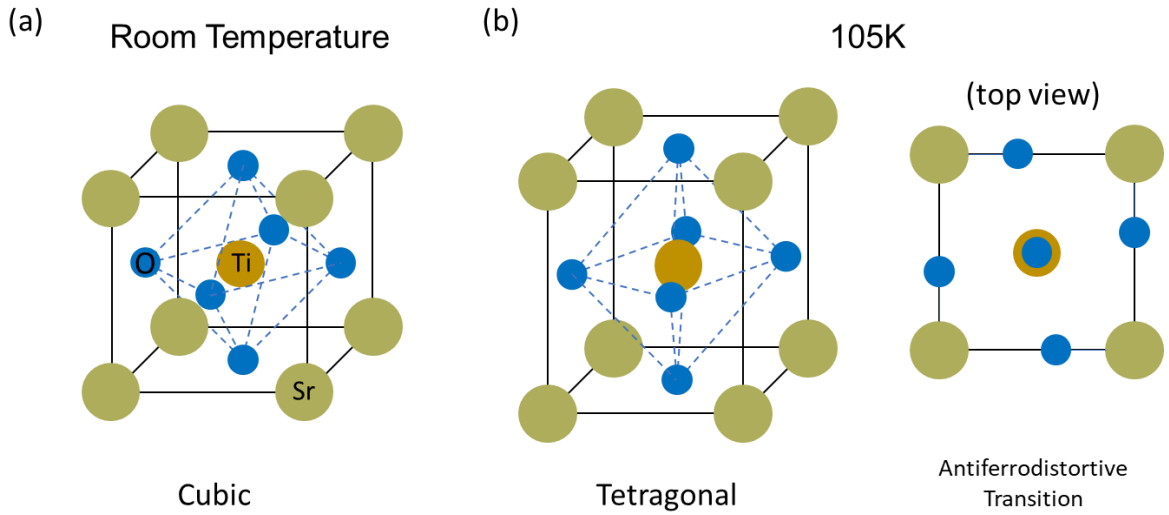

Figure 1.2. Crystal structure of $SrTiO_3$. (a) Cubic structure at room temperature, (b) tetragonal structure below 105 K and corresponding antiferrodistortive transition

1.3 Electronic Properties of $SrTiO_3$

$SrTiO_3$ is a band insulator with an indirect bandgap of 3.25 eV and a direct bandgap of 3.75 eV [11]. The bottom of the conduction band is composed of titanium 3d orbitals, and oxygen 2p orbitals mainly constitute the highest valence band [12]. The Ti 3d states are split by the crystal field and spin-orbit coupling. The cubic crystal field lets Ti 3d orbitals split into two energy states (four-fold e_g with higher energy and six-fold t_{2g} with lower energy) [6]. Taking into account spin-orbit coupling, the six-fold t_{2g} states split into two-fold Γ_7^+ with higher energy and four-fold Γ_8^+ with a lower energy. Below 105 K, the cubic structure is transformed to the tetragonal structure. Then, the Γ_8^+ states split further into two two-fold degenerate states under the tetragonal crystal field [4].

Insulating $SrTiO_3$ can be made into a conductor via several strategies. Both Sr and Ti can be substituted with dopants to produce free electrons. The Sr-site can be replaced with La [13,14], Sm [15], and Nd [16], while Nb has been used to replace the Ti-site [17,18]. Another route to introduce free electrons is to create oxygen vacancies. Reduced $SrTiO_3$ samples can be obtained via high-temperature annealing in a vacuum [19]. Alternatively, oxygen-deficient $SrTiO_3$ thin films can be grown under low oxygen partial pressure.

Figure 1.3 show the three conduction bands obtained by first-principles calculations [20]. Upon introducing the free electrons, they begin to fill the first (lowest) conduction band. The second and the third band are filled sequentially as the carrier concentration reaches critical values (X_{c1} and X_{c2}). Shubnikov de Haas(SdH) oscillations [21] and Raman scattering [22] measurements demonstrated multiple conduction bands in $SrTiO_3$.

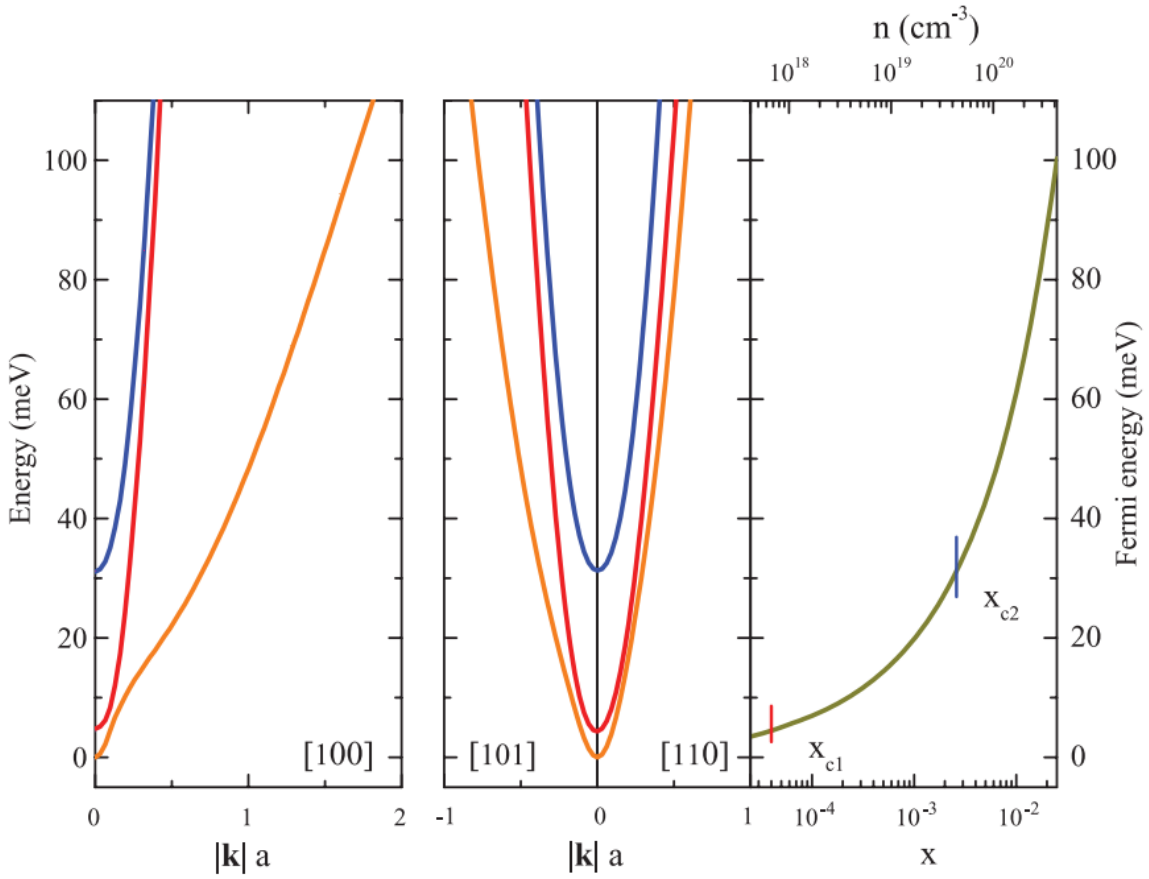

Figure 1.3. Conduction bands of tetragonal $SrTiO_3$ (left and middle panels). The band dispersions were found using first-principles calculations. **k** denotes a wavevector. The right panel shows Fermi energies depending on carrier concentrations (n). X_{c1} and X_{c2} are the critical carrier concentrations at which the second and third band begin the fill, respectively. Reprinted figure with permission from [20]. Copyright 2011 by the American Physical Society.

1.4 Ferroelectricity in $SrTiO_3$

Pure unstrained $SrTiO_3$ is paraelectric at all temperatures and is known for its high dielectric constant. The dielectric constant of $SrTiO_3$ at room temperature is ~300 and starts to increase upon cooling. The dielectric constant is sharply enhanced at low temperatures and saturated to ~20,000 below 4 K without a ferroelectric transition [23]. Because of this behavior, $SrTiO_3$ is classified as an incipient ferroelectric. Quantum fluctuations are thought to suppress the ferroelectric transition (quantum paraelectric) [24]. Further explanation follows if we consider a double potential well where the two potential wells correspond to ferroelectric states with opposite polarizations. If the depth of the potential wells is shallow enough, $SrTiO_3$ does not stay at either of the two states due to quantum tunneling between them [6].

Interestingly, it appears that $SrTiO_3$ is on the verge of a ferroelectric transition. There have been a few strategies to push $SrTiO_3$ into a ferroelectric phase through small perturbations. For example, the ferroelectric phase of $SrTiO_3$ is stabilized by the substitution of ^{16}O with ^{18}O, and fully ^{18}O substituted $SrTiO_3$ becomes ferroelectric at 23 K [25]. The heavier oxygen isotope is thought to reduce quantum fluctuations [26]. In addition, a small amount of substitution of Sr with cationic elements such as Ca [27,28], Ba [29,30], Pb [31], and Pr [32] give rise to a ferroelectric transition. For instance, the critical concentration (x_c) of Ca to induce the ferroelectric transition is 0.0018 [28]. Such low critical concentration implies that $SrTiO_3$ is in close proximity to the ferroelectric phase.

Stress and strain have been powerful tools for tailoring the properties of materials, and its effect on ferroelectricity in $SrTiO_3$ is no exception. In the 1970s, it was already reported that

uniaxial stress can induce ferroelectricity in $SrTiO_3$ [33,34]. Epitaxial strain engineering is highly effective in thin film form that is an essential ingredient for modern electronic devices. For example, tensile strained $SrTiO_3$ thin films grown on $DyScO_3$ substrates (1% lattice mismatch) showed a room temperature ferroelectric transition [35]. The polarization direction depends on the type of strain. While the polarization direction of biaxial tensile stressed films is in-plane, that of biaxial compressively stressed films is out-of-plane [35]. The ferroelectric transition temperature in electron-doped, strained $SrTiO_3$ films depends on carrier concentration. For $SrTiO_3$ films at similar thickness, the ferroelectric temperature decreases with increasing carrier density. This is because free carriers screen electric dipolar fields and, therefore, spontaneous polarization. This tendency was revealed by optical measurement (optical second harmonic generation), wherein a heavily doped film ($n \sim 3 \times 10^{20}$ cm^{-3}) lost ferroelectricity [36].

The mechanism of the ferroelectric transition of $SrTiO_3$ has been another major field of study. Generally, a ferroelectric transition is divided into the displacive type and order-disorder type. Displacive type transitions involve the abrupt displacement of atoms from their centrosymmetric equilibrium positions at the ferroelectric transition. This feature can be explained using a soft-mode model. The frequency of the lowest transverse optical (TO) phonon mode decreases (softens) as the temperature approaches the ferroelectric transition temperature, and then the frequency becomes zero at that temperature, leaving spontaneous polarization [37]. There were efforts to understand ferroelectricity of $SrTiO_3$ based on the soft-mode model [23,38].

Another type of ferroelectric transition is the order-disorder type. In this case, dipole moments persist through the ferroelectric transition temperature, but they

are disordered. As temperature decreases, they start to form long-range order, and then spontaneous polarization emerges at the transition temperature. Therefore, signature of order-disorder transition is the presence of local polarized region polar nanodomains above the transition temperature. Recently, evidence of the order-disorder type transition of $SrTiO_3$ was reported [39]. Figure 1.4 (a) and (b) show polarization vector images of unstrained and comprehensively strained $SrTiO_3$ films at room temperature, respectively. While the magnitudes of the polarization vectors in the unstrained film are small, those in the strained film are much larger. The direction of the polarization vectors of the two films is mapped on figure 1.4 (c) and (d), respectively. The strained film exhibits clear polar domains unlike the unstrained film where its polarization vectors are randomly distributed. Room temperature is much higher than the reported ferroelectric transition temperature of compressively strained thin films (~140K) [40]. Therefore, the existence of polar nanodomains above the ferroelectric transition temperature strongly supports the order-disorder type transition.

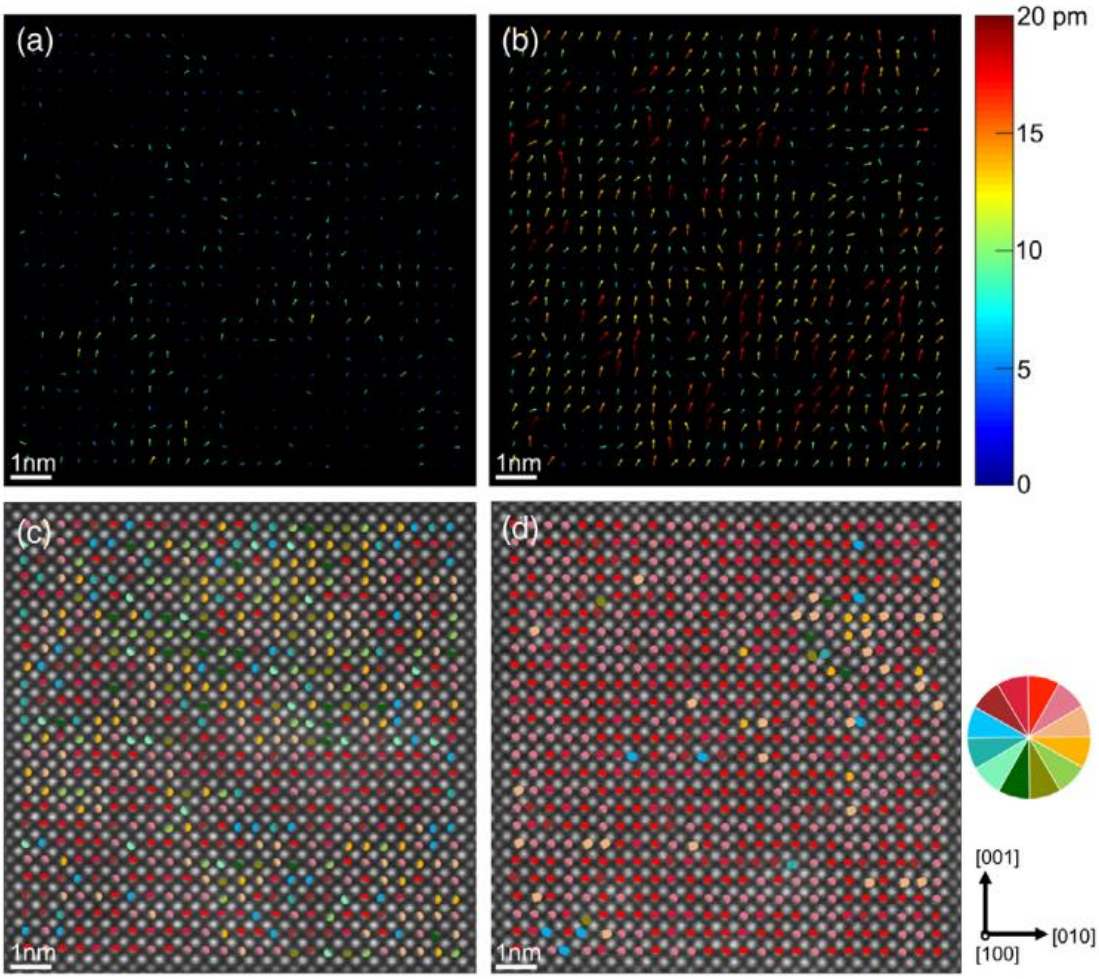

Figure 1.4. Polarization vector images of $SrTiO_3$ thin films grown on (a) $SrTiO_3$ (unstrained) and (b) LSAT (compressively strained). The polarization vectors are obtained from the displacement of Ti atoms. (c) and (d) show the directions of the polarization vectors of (a) and (b), respectively. The colors of dots on (c) and (d) are matched with the colormap which indicates the direction of the displacement vectors. Reprinted figure with permission from [39]. Copyright 2020 by the American Physical Society.

1.5 Superconductivity in $SrTiO_3$

The study of superconductivity in $SrTiO_3$ dates back to the 1960s. J. F. Schooley and W. R. Hosler reported superconductivity of oxygen-reduced $SrTiO_3$ crystals with the superconducting temperature (T_c) of ~0.3 K in 1964 [2]. Three years later, C. S. Koonce et al. reported the dependence of T_c on carrier concentrations. Interestingly, the superconducting temperatures exhibited a superconducting dome as a function of carrier concentration [3].

One of the striking superconducting properties of $SrTiO_3$ is its superconductivity at low carrier densities (~10^{17} cm^{-3}) [3,19]. This carrier density range corresponds to a Fermi energy (E_F) of ~1 meV, which is much smaller than the energy associated with the Debye frequency (ω_D). This situation leads to the violation of BCS (Bardeen, Cooper, and Schrieffer) theory. The essential condition for BCS theory is the retardation effect. Simply speaking, electron speeds must be much faster than the motion of lattice vibration for the residual positive charge due to the lattice distortion to attract another electron. Also, this effect protects electrons from strong Coulomb repulsion. Therefore, in the case of $E_F \ll \omega_D$ (anti-adiabatic), the electron pair feels the mutual Coulomb repulsion instantaneously [41], resulting in an unfavorable condition to form Cooper pairs based on BCS theory. The superconductivity of $SrTiO_3$ at the low carrier density regime makes it an attractive platform to study its unconventional superconducting characteristics.

Over several decades, there have been many theoretical approaches to explain the formation of the Cooper pairs in $SrTiO_3$ [4]. The key points of forming the Cooper pairs are reducing Coulomb repulsion between the two electrons and inducing an attractive force to

pair the electrons. For dilute (low carrier density) superconductors, the attractive force must be sufficiently strong to couple distant electrons.

GLF (Gurevich, Larkin, and Firsov) theory uses longitudinal optical (LO) modes to introduce a dynamical (frequency-dependent) screening Coulomb repulsion [42]. The theory holds for high carrier concentrations (n = ~10^{22} cm^{-3}) where $\omega_L \ll E_F$. However, this theory breaks down as the carrier concentration decreases into the anti-adiabatic regime [4]. Meanwhile, unlike dynamical screening, it was proposed that static conditions such as local polar impurities could give rise to attractive interactions [43].

As discussed in the previous section, pure $SrTiO_3$ is an incipient ferroelectric, and it is close to the ferroelectric state. Thus, small perturbations can cause spontaneous polarization. Surprisingly, the strategies which induce ferroelectricity also enhance the superconducting transition temperature. Therefore, the substitution of ^{16}O with ^{18}O [44], Ca substitution [45], and strain [15], all of which can induce ferroelectricity, were confirmed to increase the superconducting transition temperature. These results naturally let us think of the relationship between ferroelectricity and superconductivity in $SrTiO_3$. Similar to the link between spin fluctuation and superconductivity in cuprate superconductors [46], J. Edge et al. discussed the role of ferroelectric fluctuation on the superconductivity of $SrTiO_3$ [47]. The main picture of the ferroelectric fluctuation-mediated superconductivity is that the superconducting transition temperature is enhanced when the system is closer to the ferroelectric quantum critical point. This picture makes it possible to explain the superconducting dome of $SrTiO_3$ as a function of carrier density. When the Fermi surface emerges in the low carrier density regime, $SrTiO_3$ is on the verge of transitioning to a superconductor. As the carrier density increases, the system

passes through the quantum critical point (QCP). Further increase in the carrier density makes the system move away from the QCP and superconductivity is lost [48].

Meanwhile, recent experiments showed evidence of enhancement in the superconducting transition temperature inside the ferroelectric phase. Figure 1.5 exhibits the combined phase diagram of superconductivity and ferroelectricity in doped, compressively-strained $SrTiO_3$ thin films [36]. The T_c of ferroelectric, optimally doped films (~600 mK) is almost doubled compared to that of unstrained films (~300 mK). However, the T_c sharply decreases in the vicinity of the ferroelectric phase boundary. A similar observation was made in a recent single-crystal study [49]. These results call into question the role of ferroelectric fluctuations in the superconductivity of $SrTiO_3$.

The unusual aspects of the superconducting properties have been long-studied in $SrTiO_3$. For instance, superconductivity of $SrTiO_3$ is known for multiband character [16,50–52], robustness with respect to magnetic impurities [53], the theoretical prediction of odd-parity [54], and the potential of topological superconductivity [55,56]. Although superconductivity in $SrTiO_3$ was discovered in the 1960s, the challenge of understanding its nature and progressive observations of its unconventional characteristics make $SrTiO_3$ an attractive material of research.

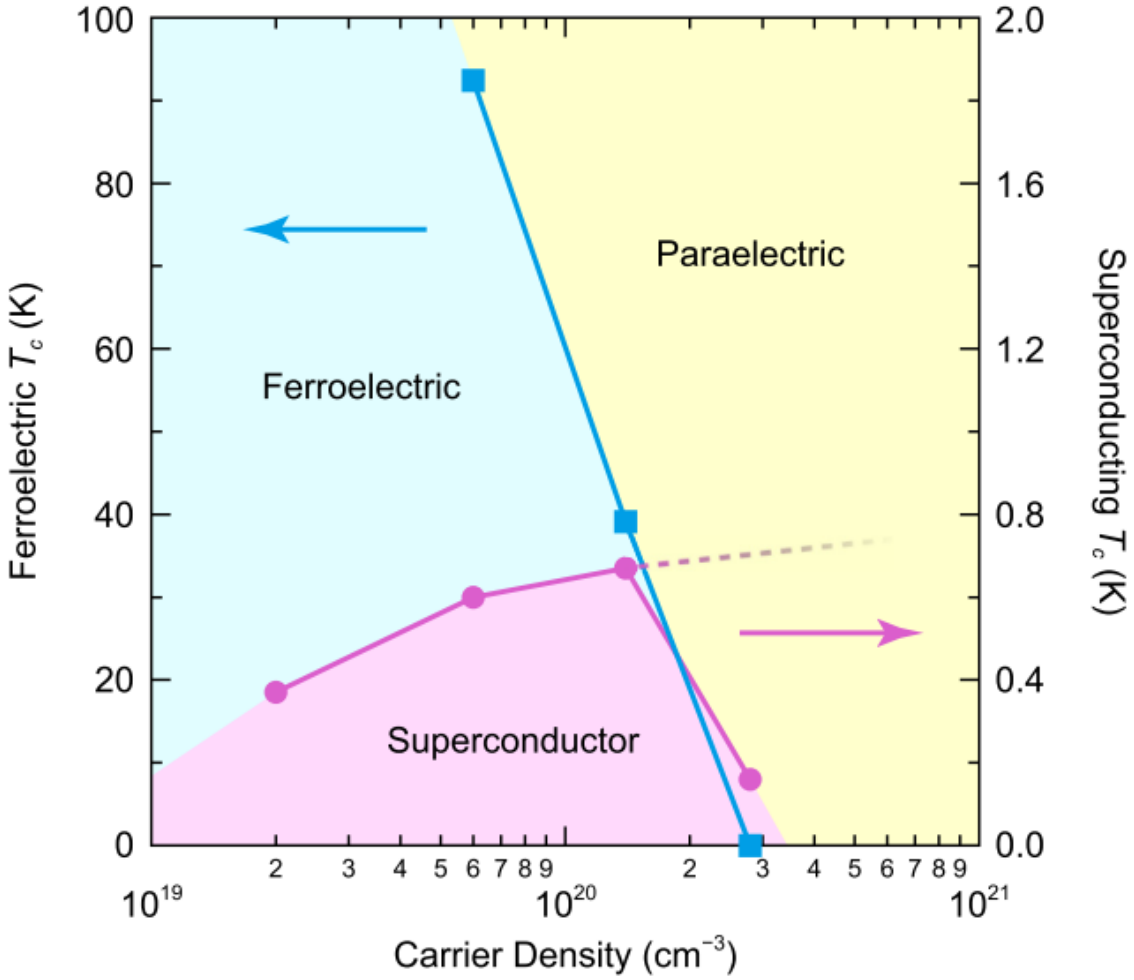

Figure 1.5 Phase diagram of superconductivity and ferroelectricity in doped, compressively strained $SrTiO_3$ films. Reprinted figure with permission from [36]. Copyright 2019 by the American Physical Society.

1.6 Outline

In Chapter 2, we introduce molecular beam epitaxy (MBE) equipment, oxide thin film growth using MBE, and examples of epitaxial growth of $SrTiO_3$ thin films. Also, basic in-situ and ex-situ characterization of the thin films are discussed.

In Chapter 3, we report the results of the superconductivity measurement of a series of ~180 nm-thick $SrTiO_3$ films. We observe a superconducting dome as a function of carrier concentration. For some films, second harmonic resistance signals are measured. We discuss the possible origin of the second harmonic resistance.

In chapter 4, we address strong surface depletion in $SrTiO_3$ thin films. Very thin $SrTiO_3$ films undergo strong carrier depletion due to their large dielectric constant at low temperatures. We solve the depletion issue with thin $EuTiO_3$ capping layers. We confirm the carrier depletion is reduced by the application of the $EuTiO_3$ capping layers and realize superconductivity in a 40-nm-thick $SrTiO_3$ thin film using the capping layer. However, we do not observe the same effect in a 10 nm-thick $SrTiO_3$ film. Possible reasons for the loss of superconductivity are discussed.

In chapter 5, we discuss why thin $SrTiO_3$ films ($<$40 nm) lose superconductivity. Based on the previous discussion regarding the connection between ferroelectricity and superconductivity in $SrTiO_3$ films, we find that both disappear at similar film thickness. We discuss the origins of the thickness-dependent results.

In chapter 6, we summarize the research results discussed in this dissertation. We also suggest future research directions that extend and develop this research area.

1.7 Permissions and Attributions

Chapter 2

MBE of $SrTiO_3$ Thin Films

2.1 Molecular Beam Epitaxy (MBE)

Molecular beam epitaxy is a thin film deposition method. MBE is characterized by ultra-high vacuum (~10^{-10} torr), high purity source materials, and low energy deposition of atoms or molecules (~0.1 eV [60]). The ultra-high vacuum condition provides a long mean free path (>1 km) and low incorporation of contaminants. The long mean free path guarantees no collisions of source atoms while they are traveling from a source cell to the substrate. Low-energy deposition is advantageous to minimize defects in crystals. Taken together, MBE is known for high quality thin film growth. MBE was first used to synthesize III-V compound semiconductors [61]. Since then, it has been widely used to grow many kinds of thin films [62].

Figure 2.1 illustrates a schematic diagram of an MBE chamber for oxide thin film growth. Chamber pressure of the ultra-high vacuum range (~10^{-10} torr) is maintained by a complex system comprising a turbopump, a roughing pump, and liquid nitrogen cooling. A residual gas analyzer (RGA) detects residual substances in the chamber as a function of molecular mass. Metal sources (strontium, lanthanum, samarium and in this dissertation) are supplied from effusion cells, and their fluxes are measured by a beam flux monitor (BFM). Oxygen gas can be independently supplied from another port, and it is often supplied as oxygen plasma for better reactivity. In this dissertation, we also used metal-organic sources. In this case, the metal-organic sources can be supplied using a gas inlet system. The gas pressure is controlled by a linear leak valve (LLV) and a Baratron gauge. A substrate on a face place is mounted on a heater assembly. The substrate heater and the source cells are heated up to their target temperature. The film growth is triggered by opening shutters.

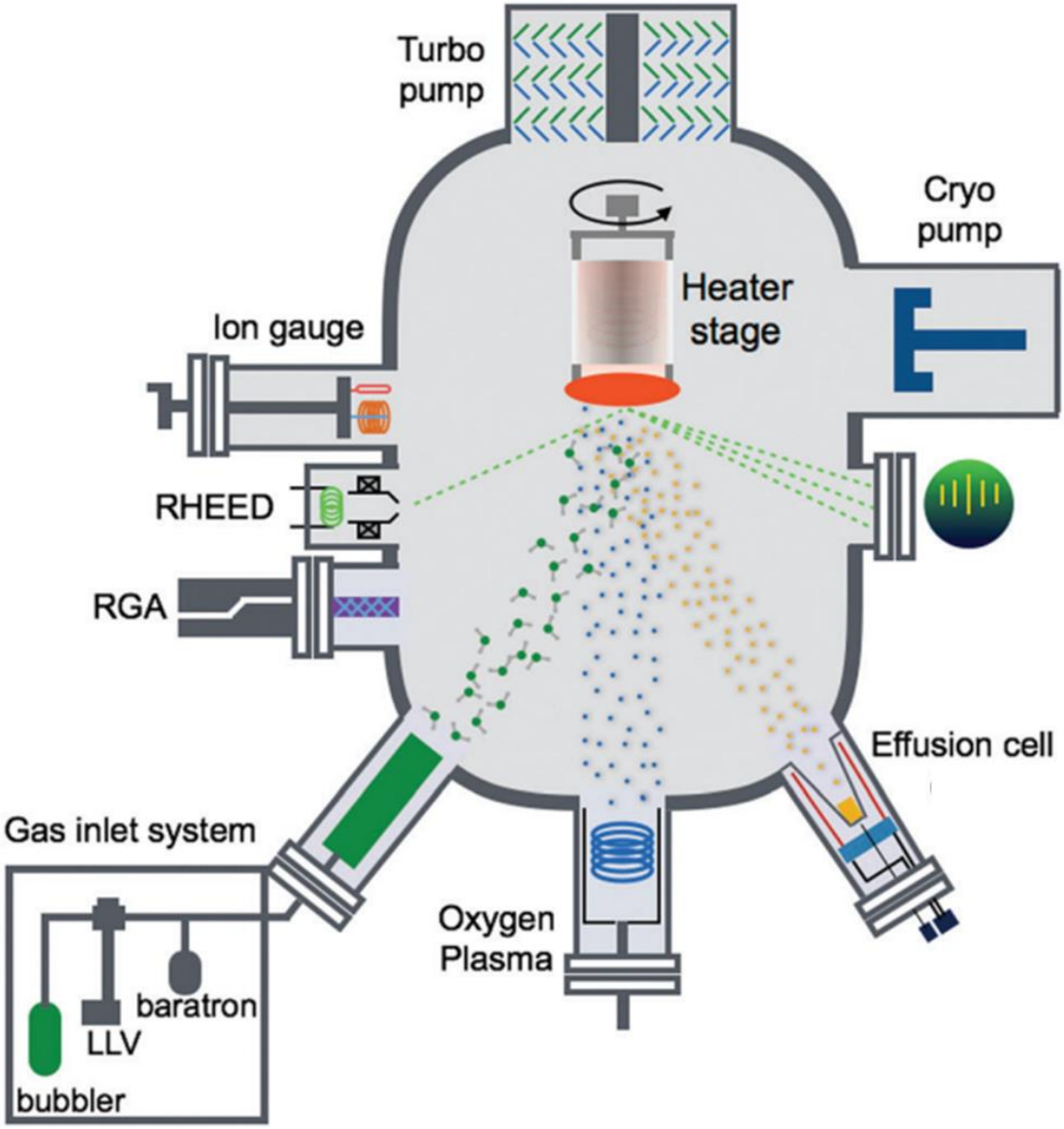

Figure 2.1 Schematic diagram of an MBE chamber with a gas inlet system for metal-organic source. Adapted from Ref. [63] with permission from the Royal Society of Chemistry.

2.2 Hybrid MBE

The success of conventional (without metal-organic sources) MBE growth of III-V compound semiconductors has been attributed to the wide growth window with respect to temperature and gas pressure [64]. However, it is challenging to grow $SrTiO_3$ thin films using the conventional approach. When metallic sources of Sr and Ti are used for the film growth, the growth window of $SrTiO_3$ becomes very narrow, and an extremely high growth temperature (~1500 K) is required to use a practical range of Sr flux (~10^{-8} torr BEP) [65,66]. The breakthrough was made by introducing metal-organic sources. In the case of $SrTiO_3$ growth, titanium tetraisopropoxide ($Ti(OC_3H_7)_4$, TTIP) has been used to replace metal Ti sources. TTIP-based growth leads to adsorption-controlled growth which gives a much wider growth window than that of conventional, solid-source growth. Furthermore, the vapor pressure of metal-organic sources is much higher than that of metal sources, which gives rise to scalable growth rates [65]. Hybrid MBE stands for the combined (conventional + metal-organic) approach. There are also other advantages of the hybrid MBE growth. Due to its high vapor pressure, TTIP does not require a carrier gas [67], and oxide thin film growth without oxygen gas is possibly due to oxygen atoms in TTIP molecules. Although there was a concern about carbon contamination in this hybrid method from TTIP, we found that it became negligible at our growth temperatures (>800°C) [68].

2.3 Epitaxial Growth of $SrTiO_3$ Thin Films Using Hybrid MBE

In this section, we elaborate on general procedures of growth of compressively strained $SrTiO_3$ thin films with some auxiliary explanations. All $SrTiO_3$ films studied in this dissertation were grown by this procedure.

First of all, we need to select the substrate on which $SrTiO_3$ films will be grown. There is a large degree of freedom of perovskite oxide substrates for the epaxial growth of $SrTiO_3$ films [7]. Given the lattice parameter of $SrTiO_3$ (3.905Å), $(LaAlO_3)_{0.3}(Sr_2AlTaO_6)_{0.7}$ (LSAT) substrates (3.868 Å) result in moderate compressive in-plane strain (~1%) on $SrTiO_3$ thin films, which also induces ferroelectricity [35,36,69]. The LSAT substrates were purchased from MTI corporation or CrysTec GmbH. The LSAT substrates are screened by x-ray diffraction (XRD). We perform rocking curves on the (001) plane to select substrates based on the peaks with the lowest full width at half maximum (FWHM). The substrates are cleaned with acetone and isopropanol in an ultrasonic bath prior to growth.

Next, a tantalum backing layer (3500 Å thick) is deposited on the backside of the substrates using an electron beam evaporator. The metal backing layer improves heat exchange between oxide substrates and the heater [67]. The substrates are cleaned once more before loading them into the MBE system (Veeco Gen 930). The substrates are loaded into the load-lock chamber and baked at 200℃.

Prior to beginning thin film growth, we measure temperature-dependent fluxes of the sources with a beam flux gauge (BFM) to determine the optimum cell temperature and TTIP pressure for $SrTiO_3$ film growth. After this process, the substrate is loaded to the MBE main chamber through a buffer chamber, and then we start to heat up the substrate and the source

cells. We outgas the source cells by heating them over the target temperatures to evaporate potential contaminants on the source surface. We run the growth recipe after the substrate temperature and the source cell temperatures are settled at the target temperatures.

Growth begins once the cell shutters are opened. The initial growth status can be monitored by in-situ reflection high-energy electron diffraction (RHEED). We check surface reconstructions and intensity oscillations using RHEED (see Ref. [70] for further information about RHEED). Figure 2.2 illustrates RHEED intensity as a function of time during the growth of a $SrTiO_3$ film. The intensity oscillations are clearly seen in the figure. These oscillations indicate the film was grown in layer-by-layer growth mode. Since one oscillation corresponds to the completion of one unit cell, we can estimate the growth rate and film thickness from the RHEED oscillation data.

Usually, RHEED signals are taken for the first five minutes, and then we rotate the substrate to improve film uniformity. When the growth recipe is finished, we inspect the static RHEED patterns. The post-growth RHEED image shows surface reconstruction related to the stoichiometry of $SrTiO_3$ films [71,72]. Figure 2.3 shows typical surface reconstructions of an $SrTiO_3$ film taken after growth. The streaky RHEED patterns in the figure indicate that the film surface is smooth without 3D islands [70]. Half-order surface reconstruction only in the <1 0 0> azimuth pattern implies that the $SrTiO_3$ film has mixed (1×2) and (2×1) surface reconstruction, which is a known surface reconstruction of stoichiometric $SrTiO_3$ films [71,72].

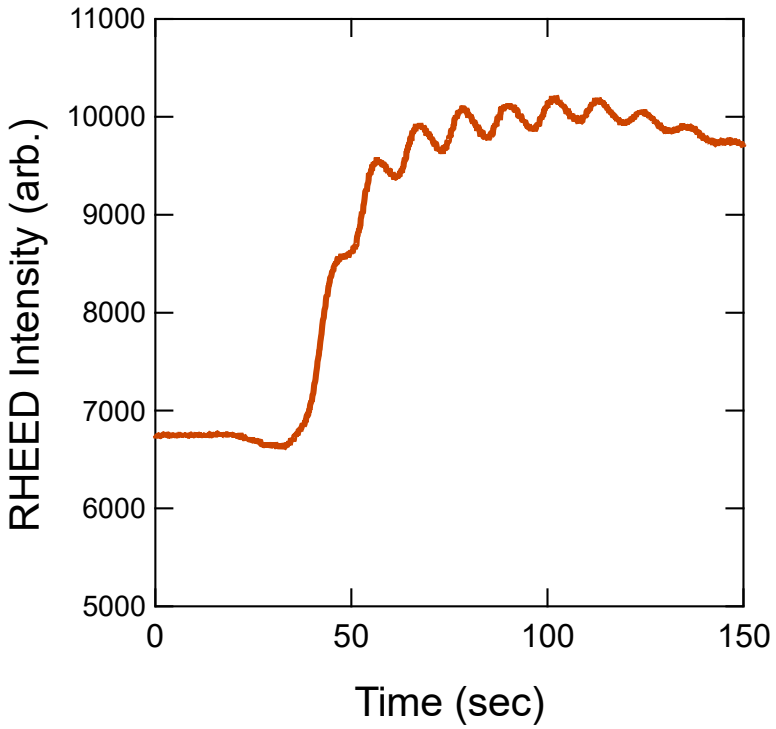

Figure 2.2 RHEED intensity as a function of time during the growth of a $SrTiO_3$ film

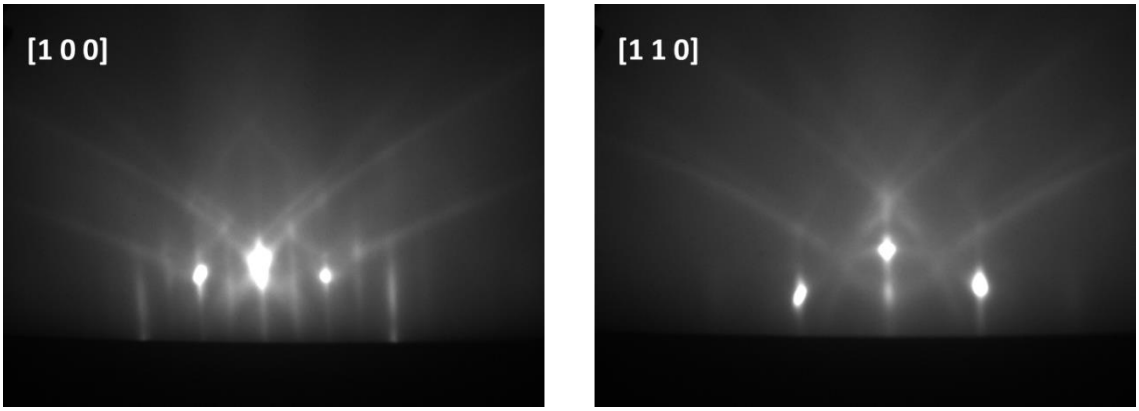

Figure 2.3 Post-growth RHEED image along the [100] (left panel) and [110] (right panel) azimuths

2.4 Ex-situ Characterizations

After film growth, the out-of-plane lattice parameter is measured using XRD. The out-of-plane lattice parameter increases due to in-plane biaxial compressive strain. XRD data of the samples in this dissertation were measured using a Panalytical X'pert thin film x-ray diffractometer. We perform on-axis 2θ-ω scans to calculate the out-of-plane lattice parameter. Before running the 2θ-ω scans, calibration XRD measurements (2θ, ω, z scans, etc.) for sample alignment are performed.

Figure 2.4 shows XRD data of a typical $SrTiO_3$ film (57 nm) grown on an (100) LSAT substrate using the growth method introduced in the previous section. The 002 LSAT reflection is sharply defined with high intensity. The 002 $SrTiO_3$ reflection is symmetric (no partial relaxation). Thickness fringes imply that the film surface is smooth. Based on the 2θ position of the film peak, the out-of-plane lattice parameter of this sample is 3.930 Å. This value matches that expected for coherently strained stoichiometric $SrTiO_3$ film grown on LSAT. A large deviation from this value would be a sign of nonstoichiometric growth conditions [65,69] or partial strain relaxation [73,74].

Electrical characterization of our $SrTiO_3$ films was performed in van der Pauw or Hall bar geometries, respectively. The van der Pauw method allows us to measure sheet resistance and carrier density using a simple geometry with minimal device fabrication. Figure 2.5 illustrates the van der Pauw geometry. The small Ohmic contacts (Ti/Au) at the four corners are deposited with electron beam evaporation using a shadow mask. Here, we define multiple resistances as

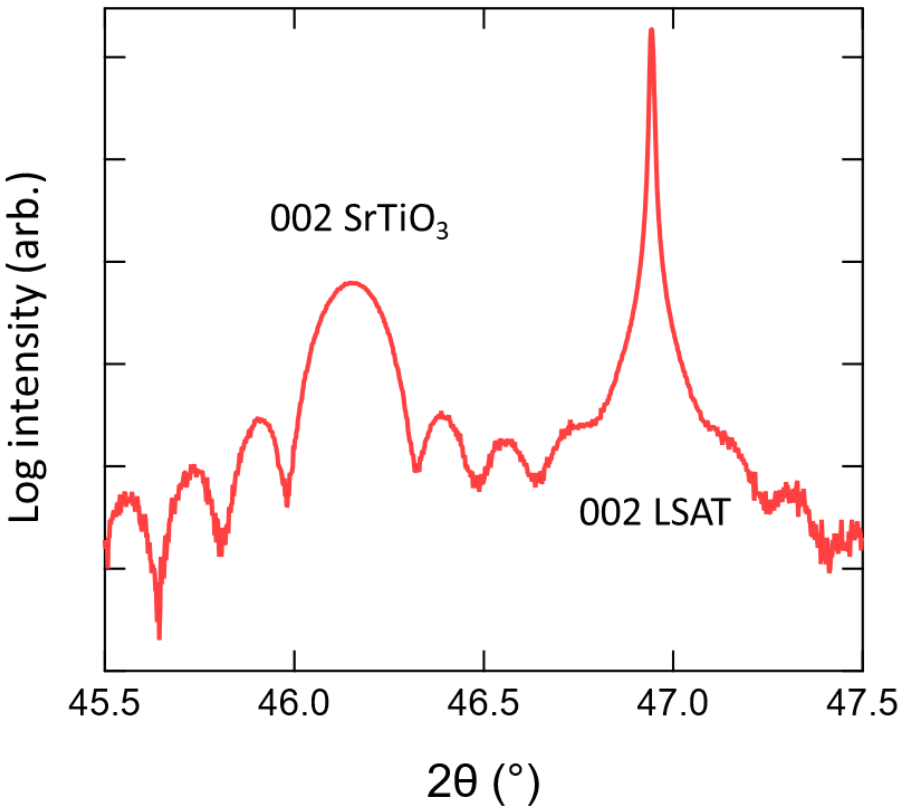

Figure 2.4 *2θ-ω* XRD scan near the 002 film reflection of a $SrTiO_3$ film on LSAT. The thickness of the $SrTiO_3$ film is 57 nm.

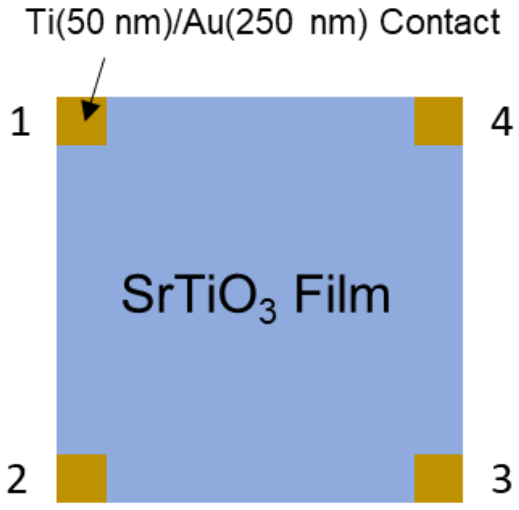

Figure 2.5 van der Pauw geometry for electrical measurements

follows: $R_A = V_{4\to3}/I_{1\to2}$, $R_B = V_{1\to4}/I_{2\to3}$. $V_{i\to j}$ and $I_{i\to j}$ represent voltage and current from the contact i to the contact j. The contact numbers are labeled in Figure 2.5. Then, the relationship between R_A, R_B, and sheet resistance (R_S) is expressed as $e^{(-\frac{\pi R_A}{R_S})} + e^{(-\frac{\pi R_B}{R_S})} = 1$ [75]. Though there is no simple expression for R_S, it can be numerically calculated. In addition, we define the Hall voltage as $V_H = V_{2\to4}$ and the sheet (2D) carrier density as $n_s = \frac{I_{3\to1}B}{q|V_H|}$, where B is the out-of-plane magnetic field, and $q = 1.602 \times 10^{-19}\ C$ [76]. The three-dimensional carrier density is obtained by diving the sheet carrier density by the film thickness. The measurements were carried out using a Quantum Design Dynacool System.

Meanwhile, Hall bars were also used for some studies in this dissertation. Hall bars are micron-scale devices that alleviate the non-uniformity of relatively large van der Pauw samples.. Figure 2.6 shows the optical micrograph image of a Hall bar. A mesa pattern is defined with eight metal contacts (Ti/Au) on top. These Hall bar devices are fabricated by photolithography, ion milling for mesa definition, and e-beam deposition of metal contacts.

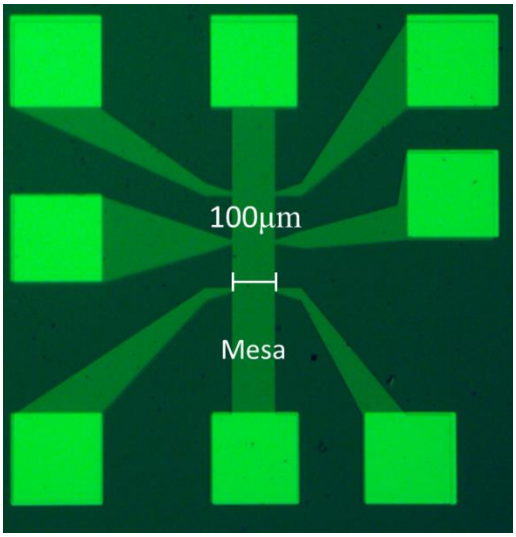

Figure 2.6 Optical micrograph image of a $SrTiO_3$ Hall bar. An eight-contact mesa structure (pale green) is defined. The bright green squares are the Ti/Au contacts.

Chapter 3

Exploring Superconductivity in Strained $SrTiO_3$ Thin Films

3.1 Introduction

In this chapter, we report on the superconductivity in relatively thick (160-180 nm) $SrTiO_3$ thin films. Compressive strain leads $SrTiO_3$ films to noncentrosymetric polar phase. Spin-orbit coupling and possible helical edge modes make noncentrosymmetric superconductors promising candidates to realize a topological superconductor [77]. Topological superconductors have drawn keen attention recently due to their potential application to quantum computing [78]. We reconfirm the superconducting dome as a function of carrier density.

Nonlinear I-V relationships are studied by measuring the second harmonic resistance. In non-centrosymmetric electronic systems, charge transport can show non-linearity under magnetic fields. This phenomenon is called magnetochiral anisotropy [79,80]. In the normal state, it is difficult to detect the nonreciprocal transport because spin-orbit coupling and magnetic energy are significantly less than the Fermi energy. However, in the case of superconductors, the superconducting energy gap is comparable with the two energies, so much more pronounced nonreciprocal transport is expected in superconducting states. When the magnetic field is perpendicular to the direction of the electric current, the nonlinear I-V relationship is given as $V = IR + \gamma I^2 RB$, where R is the resistance, γ is the strength of magnetochiral anisotropy, and B is the magnetic flux density [80].

3.2 Methods

Hybrid molecular beam epitaxy was used to grow doped $SrTiO_3$ films as introduced in Section 2.3. The $SrTiO_3$ films were grown on LSAT substrates. $SrTiO_3$ and LSAT have a ~ -1% lattice mismatch. The film thickness was estimated from RHEED intensity oscillations. The thicknesses of the films ranged from 160 nm to 180 nm. La^{3+} or Sm^{3+} were used for n-type doping. The out-of-plane lattice parameters of the films were measured using XRD. Cross-section high-angle annular dark-field imaging in scanning transmission electron microscopy (HAADF-STEM) images were taken for some samples. A Quantum Design Physical Property Measurement System was used to perform temperature-dependent longitudinal and Hall resistance measurements from 300 K to 2 K. Three-dimensional carrier densities (n_{3D}) were determined using Hall measurements at 300 K. Hall bar devices were fabricated for superconductivity measurements as described in Section 2.4. Resistance measurements at extremely low temperatures between 12 mK to 1 K were performed in a dilution refrigerator (Oxford Instruments Triton).

The nonlinear I–V relationship was probed by measuring the second harmonic resistance. Given an AC current $I = \sqrt{2}I_0 \sin \omega t$, where ω is an angular frequency and t is time, the AC voltage is :

$$V = IR + \gamma I^2 RB = \sqrt{2}RI_0 \sin \omega t + 2\gamma BRI_0^2 \sin^2 \omega t$$

$$= \sqrt{2}RI_0 \sin \omega t + \gamma BRI_0^2 (1 - \cos 2\omega t)$$

$$= \sqrt{2}RI_0 \sin \omega t - \gamma BRI_0^2 \cos 2\omega t + \gamma BRI_0^2 \qquad (1)$$

Here, we can define first and second harmonic resistances as $R^{\omega} = R$ and $R^{2\omega} = \frac{1}{\sqrt{2}}\gamma RBI_0$. Thus, the second harmonic resistance can be measured using a lock-in amplifier at the doubled

input frequency. In-house cryogenic filters were used to reduce the electron temperature and high frequency noise during measurements of the first harmonic resistances [57]. The cryogenic filters work only at frequencies below ~100 Hz. Therefore, second harmonic resistances were measured without the cryogenic filters at higher frequencies to improve the signal-to-noise ratio.

3.3 $SrTiO_3$ Film Growth Results

Figure 3.1 shows XRD data of some of the films used in this study. Some of the films like the reference film were coherently strained, but other films, like films A (n_{3D} = 6.2×10^{19} cm^{-3}) and B (n_{3D} = 7.2×10^{19} cm^{-3}), were partially relaxed. Since the experimental critical thickness for strain relaxation is known to be ~180 nm [81], $SrTiO_3$ films with thicknesses close to the critical value undergo partial strain relaxation. Figure 3.2 shows HAADF-STEM images of the interfaces between $SrTiO_3$ and LSAT of the partially strained sample (film B). Unlike a typical well-defined $SrTiO_3$/LSAT interface (Figure 3.2c), there are slightly disordered interfacial regions in film B (Figures 3.2a and 3.2b).

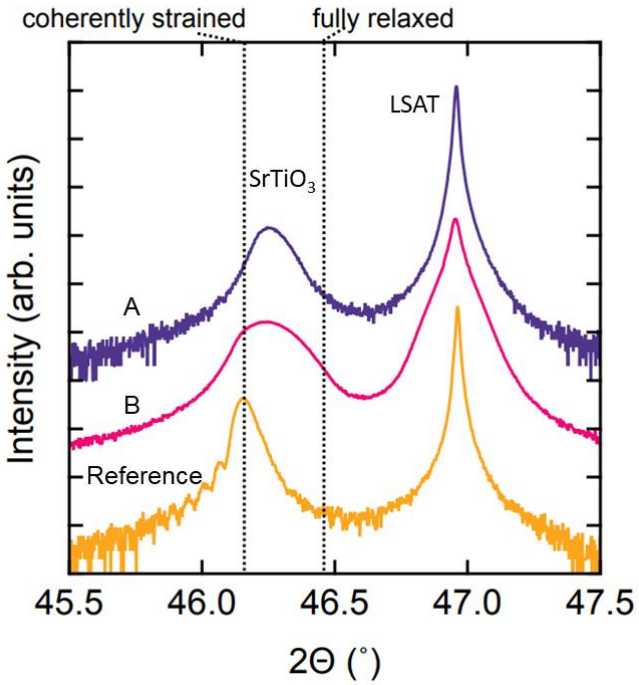

Figure 3.1 XRD patterns near the 002 film reflection of $SrTiO_3$ films on LSAT. The ideal peak positions of coherently strained and fully relaxed $SrTiO_3$ films are indicated by the dashed lines. Adapted figure with permission from [57]. Copyright 2020 by the American Physical Society.

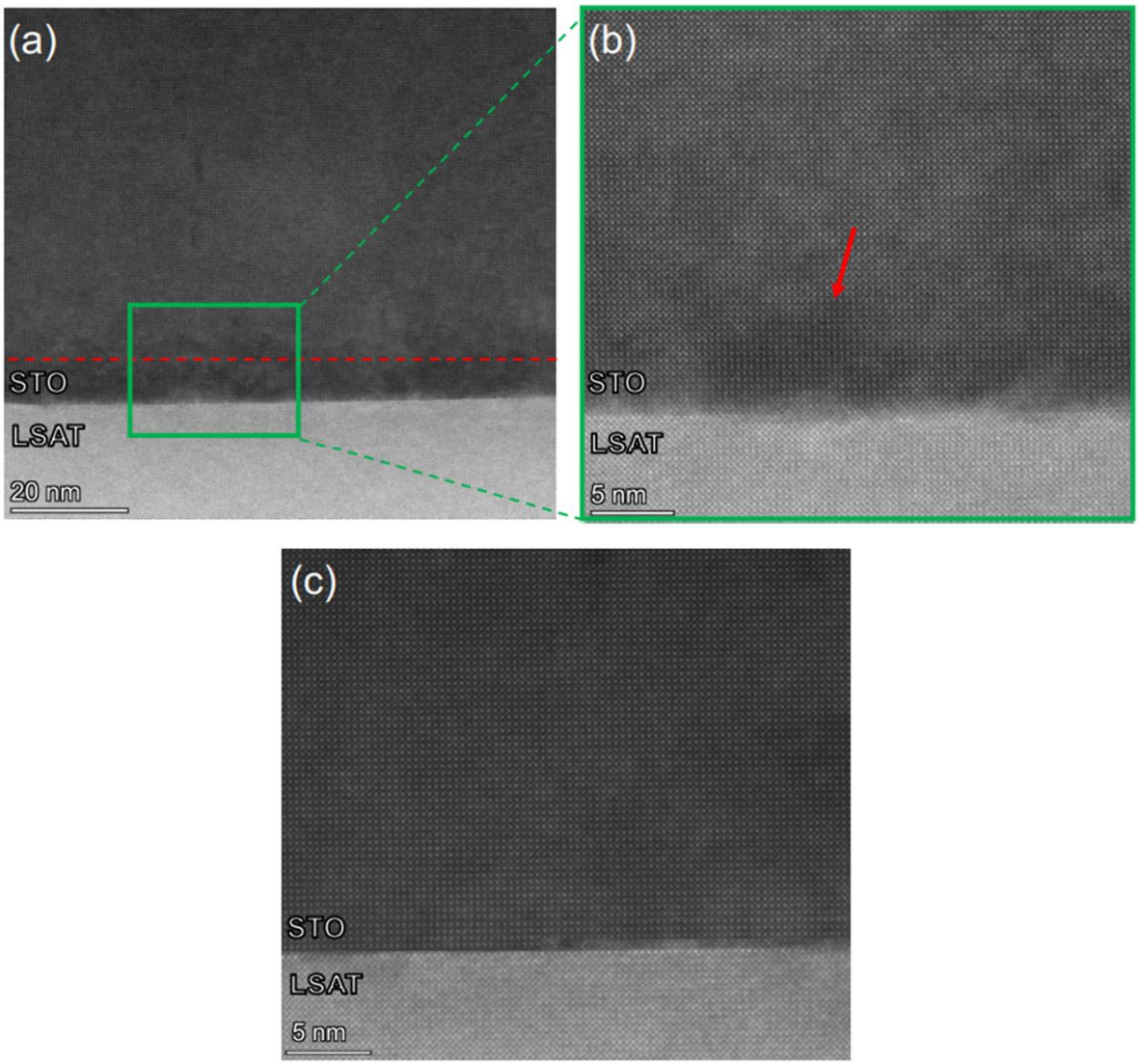

Figure 3.2 (a) Cross-section HAADF-STEM image of film B. (b) A magnified image of (a) (the magnified region is indicated by a green box in (a)). (c) Cross-section HAADF-STEM image of a strained $SrTiO_3$ film with a well-defined interface. Adapted figure with permission from [57]. Copyright 2020 by the American Physical Society.

3.4 Superconducting Properties of the $SrTiO_3$ Thin Films

Figure 3.3 shows the T_c values of the samples with various carrier densities. Here, T_c is defined as the temperature at which the sample resistance is 5% of the normal-state resistance. We note that the tendency of the T_c is similar to the results reported in an early study of doped, strained $SrTiO_3$ films on LSAT [15]. The carrier density profile of T_c forms a superconducting dome, and the maximum T_c values are ~600 mK, almost twice as high as those of unstrained films. The steep decline in T_c at lower carrier concentrations is due to the strong surface depletion effects of $SrTiO_3$ thin films [58,82]. The enhanced T_c values are closely related to the ferroelectric ground state considering the range of carrier densities where ferroelectricity exists [15,36]. Films A and B, which are partially relaxed, have a slightly lower T_c, but they are still enhanced compared to those of unstrained films.

Figure 3.4 depicts the upper critical field (H_{c2}) as a function of n_{3D}. H_{c2} is defined here as the magnetic field at which the sample resistance is 95% of the normal-state resistance. We focus on the underdoped region for sheet carrier concentrations ranging from 5×10^{19} cm^{-2} to 9×10^{19} cm^{-2}. Overall, H_{c2} tends to increase with n_{3D} in the underdoped region of the superconducting dome. We observe that H_{c2} is greatly enhanced under in-plane magnetic fields. Some samples become normal conductors at $\mu_0\mathbf{H}$ above 2 T, where μ_0 is the permeability of vacuum, and **H** is the magnetic field. The critical fields are similar to the highest reported values for doped $SrTiO_3$ [83]. Interestingly, the H_{c2} value of film B, which has disordered interfacial regions unlike film A, is the highest at ~3.5 T. Therefore, the interfacial region in film B could play a role in unusually high in-plane H_{c2}.

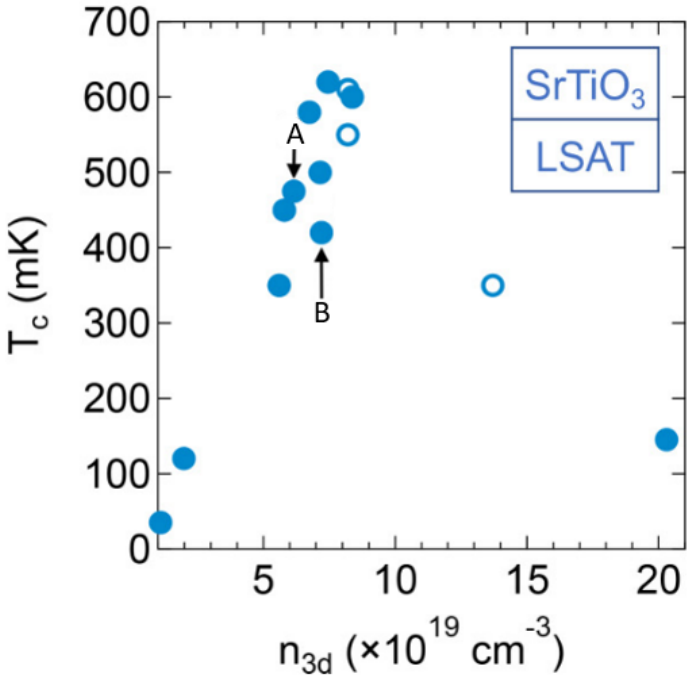

Figure 3.3 Superconducting transition temperature (T_c) as a function of n_{3D}. The open circles are Sm-doped films and the solid circles are La-doped films. Adapted figure with permission from [57]. Copyright 2020 by the American Physical Society.

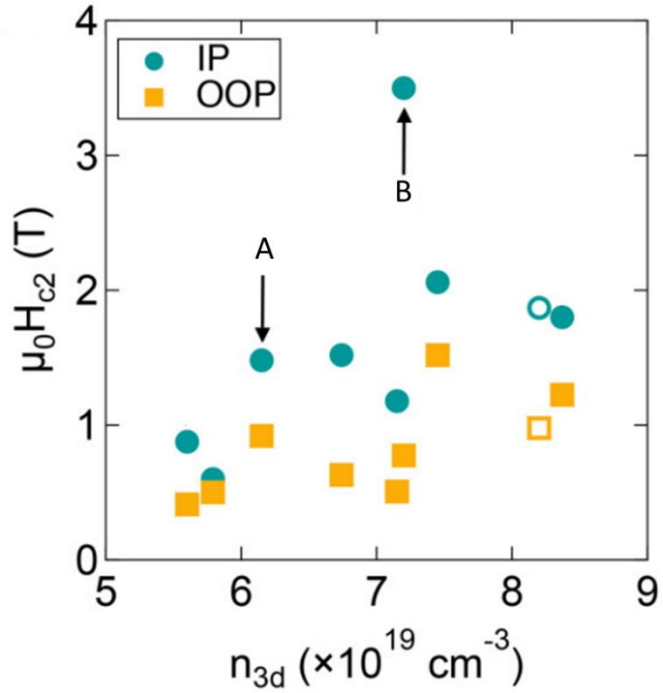

Figure 3.4 Upper critical field (H_{c2}) as a function of n_{3D}. IP and OOP stand for in-plane and out-of-plane, respectively. Open (solid) symbols are Sm-doped (La-doped) films. Adapted figure with permission from [57]. Copyright 2020 by the American Physical Society.

Next, we discuss the high H_{c2} the samples. The Pauli limiting field is obtained by equating the condensation energy of the Cooper pairs with the magnetic polarization energy of the spin-singlet state [84]. This limiting field is expressed as 1.85 T/K in units of $\mu_0 H/T$. Figure 3.5 shows the ratios of $\mu_0 H_{c2}$ to T_c. The Pauli limiting field is indicated by the dotted line. While the ratio of out-of-plane H_{c2} over T_c is smaller than the Pauli limit for most films, the ratio of in-plane H_{c2} over T_c is greater than the Pauli limit for many films. The ratio for film B is particularly high. The violation of the Pauli limit and the strong anisotropic H_{c2} are usually considered signs of spin-triplet superconductivity [54]. However, it should not be regarded as the sole source of evidence for materials with special conditions such as thin films [83,85,86], strong spin-orbit coupling [87], and multiband superconductors [16,52].

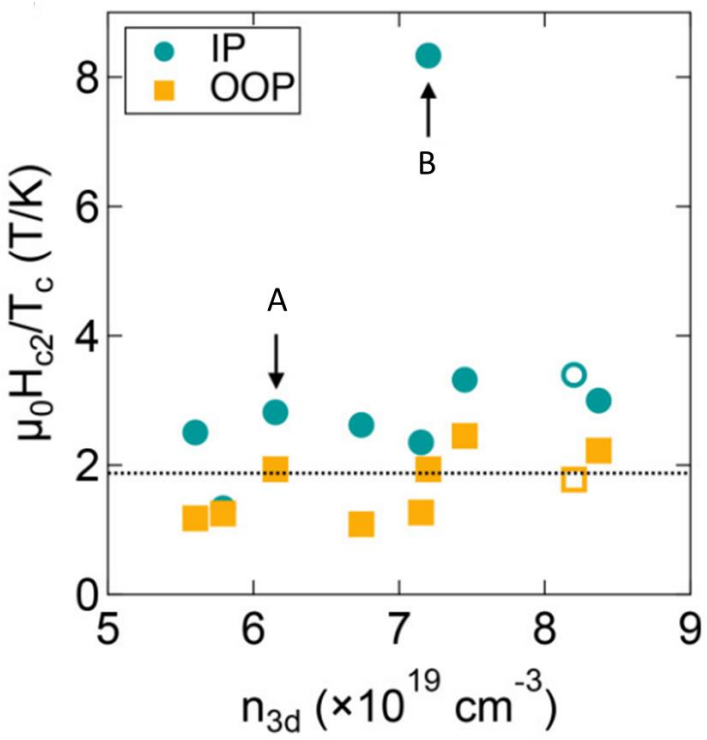

Figure 3.5 $\mu_0 H_{c2}/T_c$ values as a function of n_{3D}. IP and OOP stand for in-plane and out-of-plane, respectively. Open (solid) symbol are Sm-doped (La-doped) films. Adapted figure with permission from [57]. Copyright 2020 by the American Physical Society.

3.5 Second Harmonic Resistance Measurement

In this section, we report on the results of the second harmonic resistance ($R^{2\omega}$) measurements as evidence of nonreciprocal transport. In spin-orbit-coupled, noncentrosymmetric Rashba superconductors, non-zero second harmonic resistances can be taken as important evidence for unconventional superconductivity [88]. This is because the magnetochiral anisotropy coefficient γ is proportional to the product of the spin-orbit coupling strength and the ratio between odd-parity and even-parity Cooper pairs [88]. Thus, the nonzero resistance implies that the measured sample has at least mixed-parity superconductivity.

Figure 3.6 shows second harmonic resistances of film A. The applied magnetic field is perpendicular to the electric current. The data were antisymmetrized via $R^{2\omega}_{asym}(H) = \frac{1}{2}[R^{2\omega}(+|H|) - R^{2\omega}(-|H|)]$. The signal is purely imaginary, and the γ coefficient for this film is calculated as (1.6±0.5) × 10^3 $T^{-1}A^{-1}$. We calculated the error using error propagation and a conservative estimate of the errors in measured parameters.

We measured non-reciprocal transport on six different films. Large second harmonic resistance signals were detected from only the two partially relaxed films (films A and B). Figure 3.7 shows a comparison between the partially relaxed film (film B) and the fully strained reference film. The T_c of the reference film is high at 600 mK. The film is also ferroelectric, with a carrier density of n_{3D} = 7.2×10^{19} cm^{-3}. Nevertheless, there is no signal in the reference film above noise level. Figure 3.8 shows the antisymmetrized second harmonic resistance of film B under an in-plane magnetic field, parallel to the direction of electric

current. Given the large second harmonic resistances — up to ~50 mΩ — for $\boldsymbol{H} \perp \boldsymbol{I}$, the second harmonic signals under $\boldsymbol{H} \parallel \boldsymbol{I}$ do not seem appreciable.

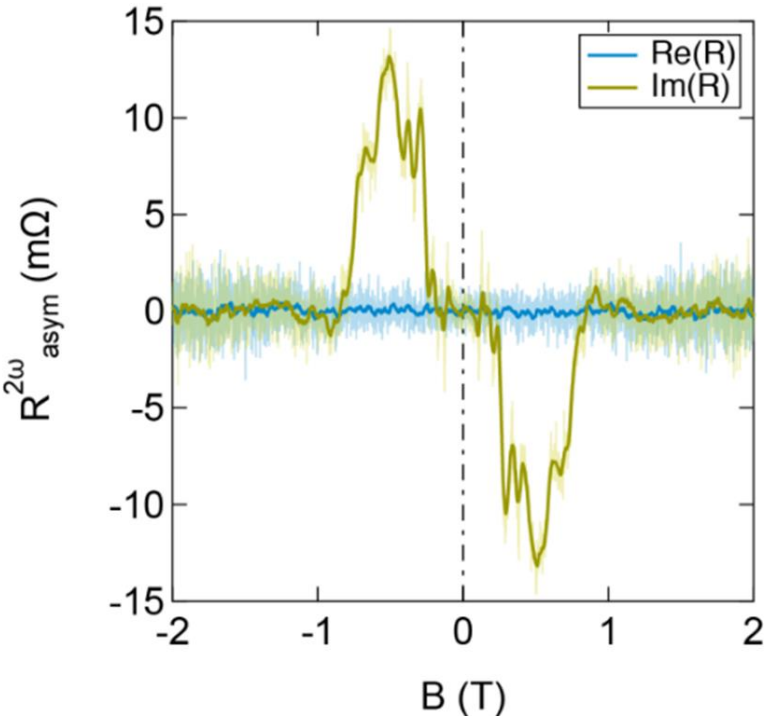

Figure 3.6 Magnetic field dependence of second harmonic resistance (Film B). Re and Im represents real and imaginary part of the resistance. Adapted figure with permission from [57]. Copyright 2020 by the American Physical Society.

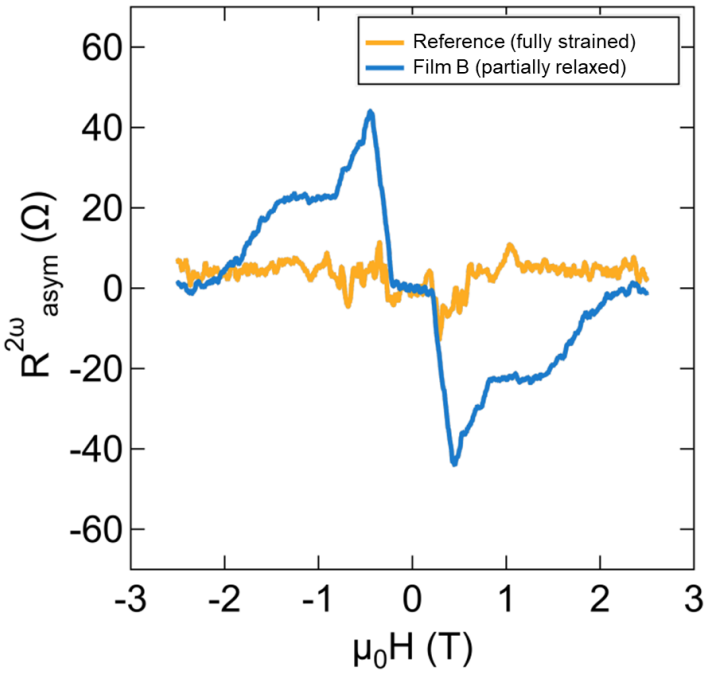

Figure 3.7 Antisymmetrized second harmonic resistance of film B (partially relaxed) and the reference film (fully strained) as shown in Figure 3.1. Adapted figure with permission from [57]. Copyright 2020 by the American Physical Society.

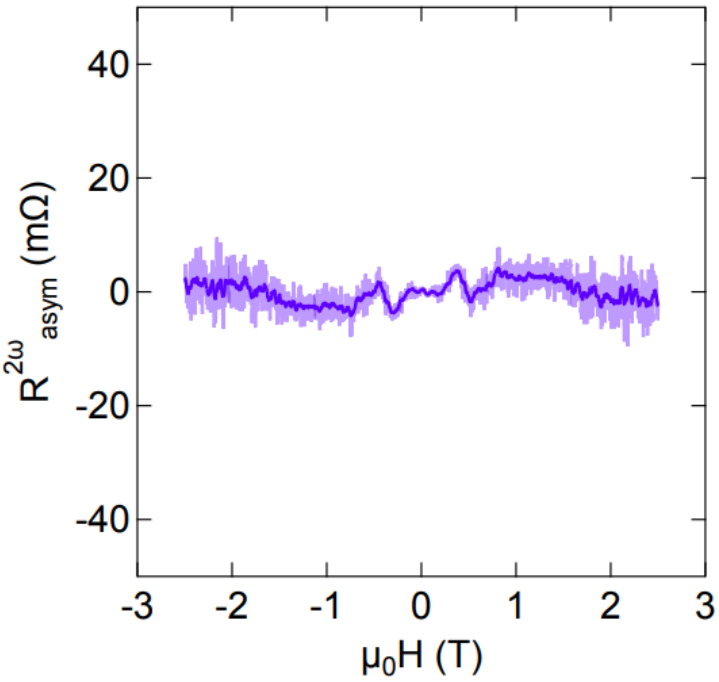

Figure 3.8 Antisymmetrized second harmonic resistance under the magnetic field parallel to the electrical field direction (film B). The darker line indicates the data after smoothing. Reprinted figure with permission from [57]. Copyright 2020 by the American Physical Society.

Next, we investigated the temperature dependence of the second harmonic resistance. Figure 3.9 shows $R_{asym}^{2\omega}$ of film B as a function of temperature. The signal weakens with increasing temperature and starts to disappear at temperatures above 300 mK. The temperature dependence of the γ parameter is shown in Figure 3.10. First harmonic resistances were measured in the same measurement setup to calculate the γ parameter. The γ parameter increases as temperature decreases, and the greatest γ value is $(4.7 \pm 0.5) \times 10^3\ T^{-1}A^{-1}$ at 12 mK. Notably, the γ value is 6 times that reported in MoS_2 [80] and twice that reported for a two-dimensional electron gas at a $LaAlO_3/SrTiO_3$ interface [89].

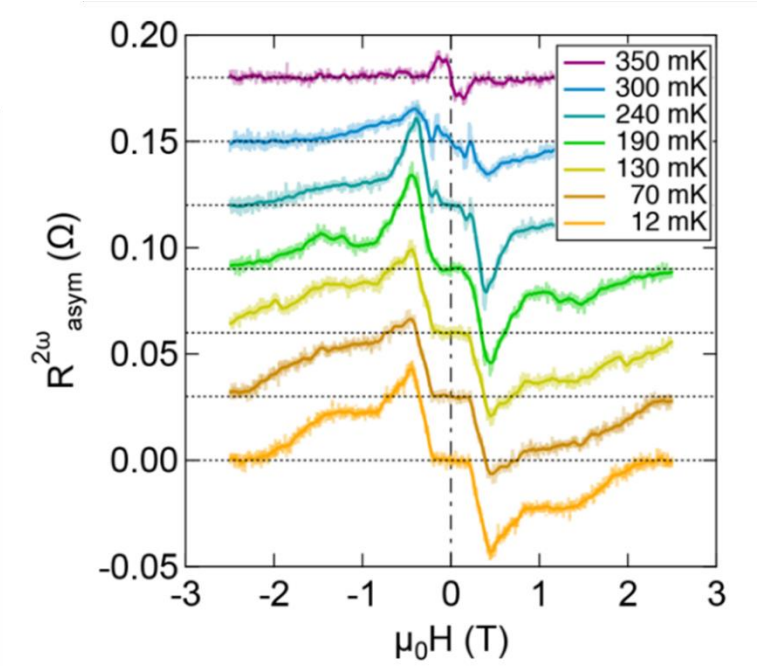

Figure 3.9 Antisymmetrized second harmonic resistance as a function of temperature (film B). The darker line indicates the data after smoothing. Reprinted figure with permission from [57]. Copyright 2020 by the American Physical Society.

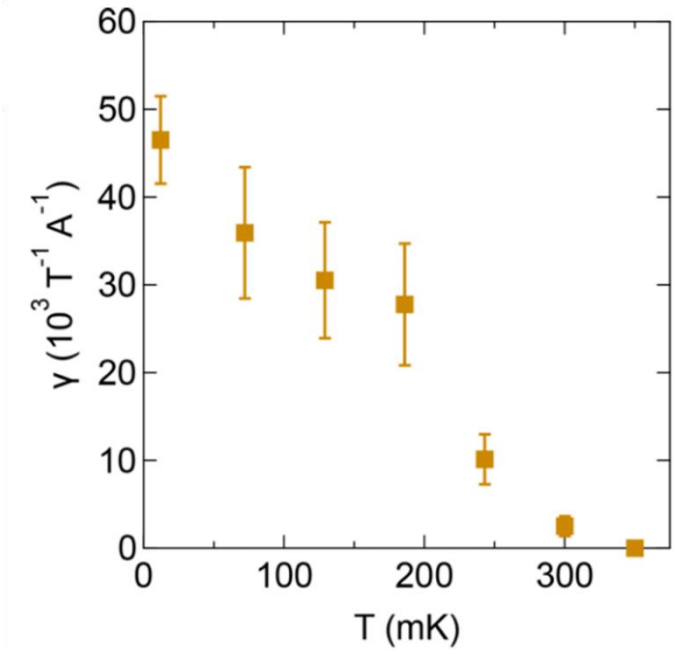

Figure 3.10 Extracted γ parameter as a function of temperature. Error bars were estimated via error propagation from the standard deviation of measured parameters. Adapted figure with permission from [57]. Copyright 2020 by the American Physical Society.

As mentioned above, the finite second harmonic resistance has been taken as a sign of mixed parity superconductivity. However, in this study, the finite signals appeared in only partially strained films (films A and B). Coherently strained, noncentrosymmetric films exhibited no detectable second harmonic resistance signal (nonreciprocal current) as shown in Figure 3.7. These results imply that inversion symmetry breaking is not a sufficient condition to generate large nonreciprocal currents in doped, strained $SrTiO_3$ films with out-of-plane polarization [36]. Therefore, other microscopic parameters appear to be important in determining the nature of superconductivity. As discussed above, the unusually high in-plane H_{c2} and the large γ value of film B appear to arise from the interfacial disordered region. In the case of the nonreciprocal transport, however, it is not purely an interface effect because it is also found in film B, which lacks an interfacial layer. The common feature of the two films

is partial strain relaxation. Theoretical studies that elucidate the role of interfaces, electronic structure, dimensionality, and strain gradients would be a key step toward better understanding and modifying the superconducting properties in $SrTiO_3$ films.

3.5 Discussion and Conclusion

Doped, compressively strained, polar $SrTiO_3$ films have been grown by hybrid molecular beam epitaxy and their superconducting properties have been studied. The maximum T_c reaches ~600 mK as reported elsewhere [15]. The in-plane H_{c2} of many films in the underdoped region is greater than the Pauli limiting field. We find that some of the $SrTiO_3$ films exhibit the signature of spin-orbit coupled, noncentrosymmetric superconductors. Partially relaxed films show large second harmonic resistance under the magnetic field perpendicular to the current direction. This result supports that the nonreciprocal transport is mediated by magnetochiral anisotropy.

Although the nonreciprocal transport might come from parity mixing of Cooper pairs [88], recent studies have focused on the role of vortex motion in nonreciprocal transport in noncentrosymmetric systems [90,91]. Our result is not fully explained by the vortex motion. Based on the vortex motion scenario, the γ parameter should be suppressed in zero-resistance states, but the γ parameter in this study increases as temperature decreases down to the base temperature (12 mK). Therefore, further studies were necessary to better understand the nonreciprocal transport in these films.

Chapter 4

Reducing Surface Depletion of Superconducting $SrTiO_3$ Films

4.1 Surface Carrier Depletion in $SrTiO_3$ Thin Films

As discussed in the previous chapters, strained $SrTiO_3$ film undergo subsequent ferroelectric and superconducting transitions as temperature drops. Therefore, these films are a good platform to study the mutual interaction between ferroelectricity and superconductivity. The surface depletion of air-exposed $SrTiO_3$ is likely induced by chemisorption of oxygen-containing, electronegative, molecules [92,93]. It is known that the depleted layer can be eliminated by heating in a vacuum [68] or electromagnetic radiation [93,94]. These approaches are impractical for most applications, however, which necessitate devices that operate in ambient conditions.

The width of the surface depletion is given as

$$d = \sqrt{2\varepsilon\varepsilon_0\Phi_B/en_{3D}} \quad (2)$$

where ε, ε_0 are dielectric constant (relative permittivity) of $SrTiO_3$ and permittivity of vacuum, respectively. Φ_B, e, n_{3D} are surface pinning potential (surface barrier height), the electron charge, and 3D carrier density, respectively. Ohtomo et al. studied the surface depletion in $SrTiO_3$ films extensively as a function of film thickness and temperature, and Φ_B of 0.7 eV was suggested [82]. As predicted from equation (2), the surface depletion region expands as the dielectric constant increases. In this regard, $SrTiO_3$ thin films undergo severe surface depletion due to the very large dielectric constant (ε = ~ 20,000) at low temperature [23].

Figure 4.1 shows an example of the carrier density dependence of the depletion layer width at low temperature where the dielectric constant can be assumed as ~20,000. The depletion width increases sharply in the low carrier density region. Since one of the unique properties

of $SrTiO_3$ is dilute superconductivity, the strong surface depletion has been a major obstacle to studying superconductivity in $SrTiO_3$ thin films.

To avoid complete depletion, thin films must be significantly thicker than the depletion layer width [95,96]. However, for strained $SrTiO_3$ films, the required film thickness can exceed the critical thickness for strain relaxation. Furthermore, surface depletion results in a non-uniform carrier density across the film thickness. The non-uniform carrier distribution along with carrier concentration dependence of T_c can make it challenging to interpret the observed change in T_c. Therefore, it is necessary to develop capping layers that reduce or prevent surface depletion. The dielectric constant of ferroelectric films will be smaller than that of paraelectric films since ferroelectric transition involves a reduction in the dielectric constant [35], so the capping layer could be less effective in ferroelectric films compared to paraelectric films.

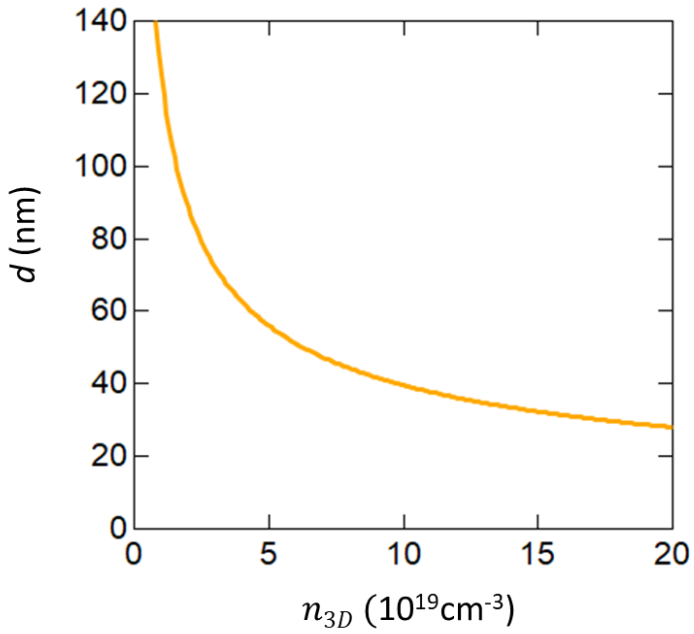

Figure 4.1 Estimated width (d) of the depletion layer in $SrTiO_3$ film as a function of carrier densities at low temperature. Fitting parameters were referred from Ref. [97].

4.2 $EuTiO_3$ as a capping material

In this study, $EuTiO_3$ is used as an effective capping layer on $SrTiO_3$ to reduce the surface depletion. $EuTiO_3$ is another well-known perovskite cubic oxide with a lattice parameter of 3.908Å. $EuTiO_3$ undergoes tetragonal transition similar to $SrTiO_3$ [98]. The lattice parameter of $EuTiO_3$ is very close to that of $SrTiO_3$ (3.905Å). Therefore, nearly strain free epitaxial growth between $EuTiO_3$ and $SrTiO_3$ is possible. At low temperatures, $EuTiO_3$ becomes antiferromagnetic (G-type) with a Néel temperature of 5.5K [99]. Figure 4.2 illustrates the spin configuration of G-type antiferromagnetism. Because the magnetic moments are canceled out, it is expected that the magnetic order in $EuTiO_3$ will have a negligible effect on the superconducting properties of $SrTiO_3$.

When it comes to surface carrier depletion, $EuTiO_3$ is advantageous due to its relatively low dielectric constant (< 400) at low temperatures [100]. $SrTiO_3$-based perovskite oxide heterostructures often create two-dimensional electron gas at their interface because of polar discontinuity [101,102]. However, Eu with a +2 valence state in $EuTiO_3$ does not result in the polar discontinuity. Therefore, superconductivity in $SrTiO_3$ films with $EuTiO_3$ capping layer is not affected by external two-dimensional electron gas.

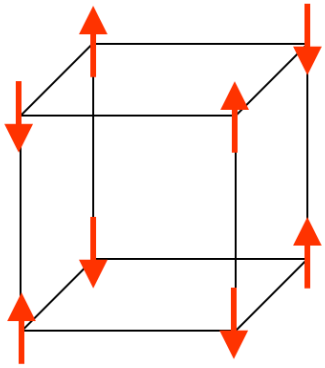

Figure 4.2 G-type antiferromagnetism

4.3 MBE of Strained $EuTiO_3$ Thin Films

Prior to applying $EuTiO_3$ capping layers on $SrTiO_3$ thin films, we performed calibration growth of $EuTiO_3$ thin films. Compressively strained $EuTiO_3$ thin films were grown on (001) LSAT substrates. The growth method of $EuTiO_3$ thin films is very similar to that of $SrTiO_3$ films, as introduced in Chapter 2, aside from replacing Sr source with Eu source. The Eu cell temperature was adjusted at ~ 450℃ to get the same flux as that of Sr that was used in $SrTiO_3$ film growth. The thermocouple temperature of a substrate heater was 1000℃. The growth condition was optimized by controlling the ratio between Eu flux and TTIP pressure.

Figure 4.3 shows RHEED oscillations during the growth of a $EuTiO_3$ film on an LSAT substrate. The initial growth mode is a layer-by-layer growth. Figure 4.4 shows a typical RHEED image of $EuTiO_3$ film taken after growth. The surface reconstruction pattern shown in the figure is very similar to that of $SrTiO_3$ (Figure 2.3). The smooth film surface is demonstrated by the streaky RHEED patterns.

The strained $EuTiO_3$ film quality was inspected using XRD (Figure 4.5). The out-of-plane lattice of the film is 3.931Å which is the same as that of the previously reported high quality strained $EuTiO_3$ film grown by hybrid MBE [103]. Thickness fringes are clear as well.

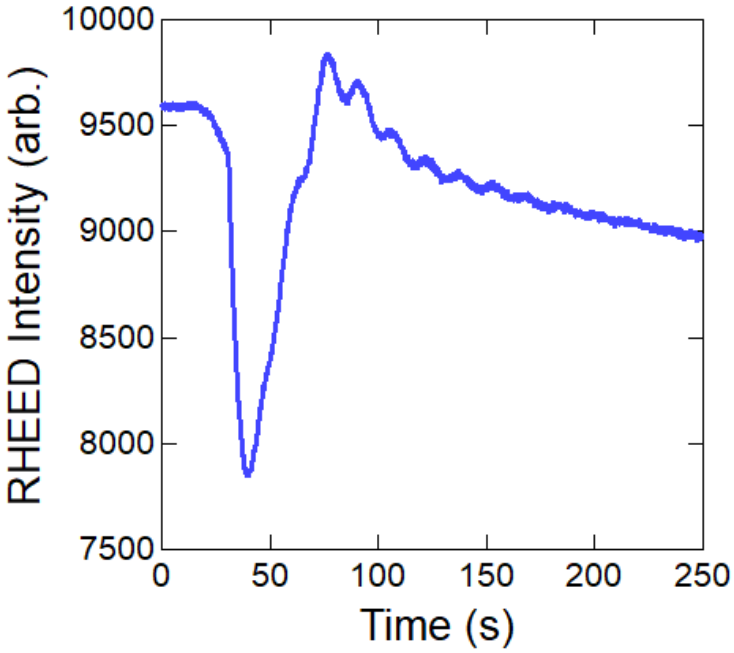

Figure 4.3 RHEED intensity oscillations measured at the beginning of (001) $EuTiO_3$ film growth. The film growth mode was initially layer-by-layer growth mode.

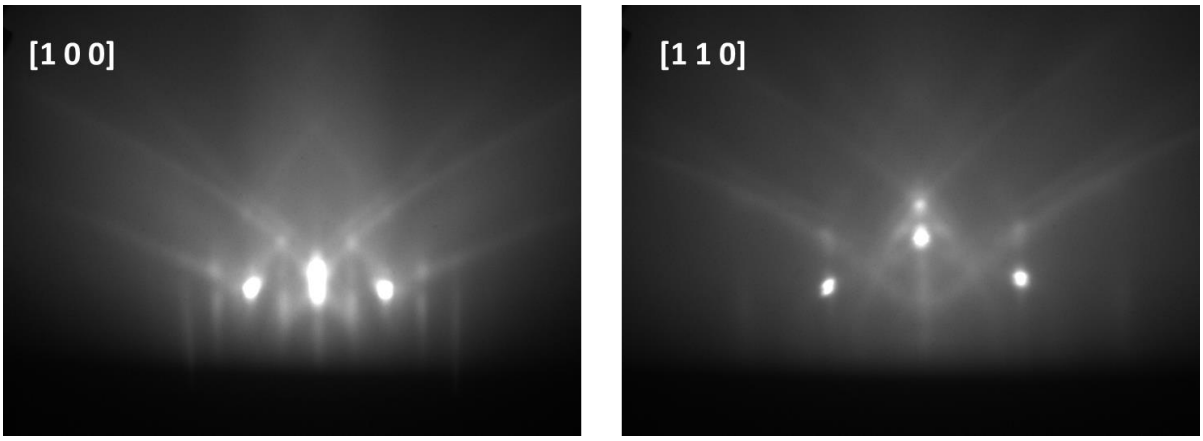

Figure 4.4 Post-growth RHEED image of an $EuTiO_3$ film along the [100] (left panel) and [110] (right panel) azimuths.

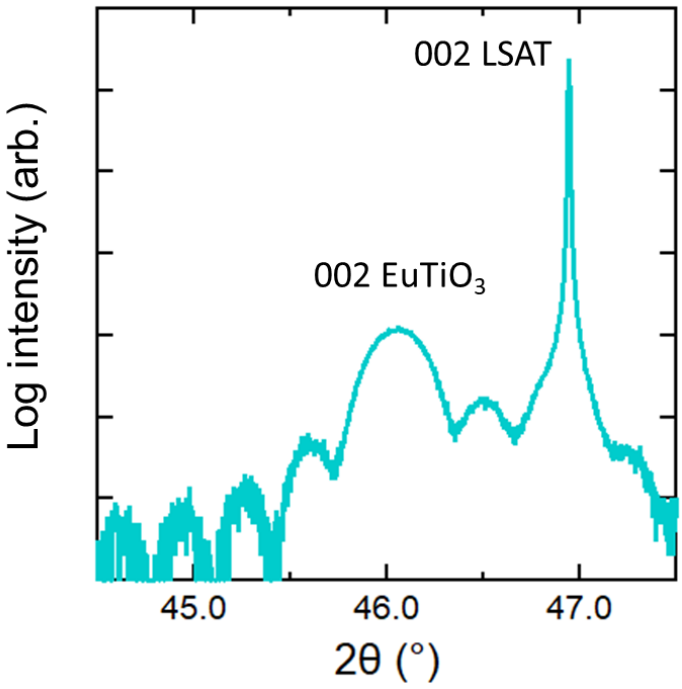

Figure 4.5 XRD patterns near the 002 film reflection of a $EuTiO_3$ film on LSAT substrate. The film thickness is 30nm.

4.4 MBE of Strained $EuTiO_3/SrTiO_3$ Heterostructures

Coherently strained, doped $EuTiO_3/SrTiO_3$ thin film heterostructures were grown by hybrid molecular beam epitaxy based on the calibrated growth condition [67,104]. The samples studied here had a $EuTiO_3$ layer thickness of 10 nm, while the thicknesses of the $SrTiO_3$ layer were varied to correspond to 70 nm (sample A), 40 nm (sample B), and 10 nm (sample C). The oxide heterostructures were grown on (001) LSAT substrates, and both $SrTiO_3$ and $EuTiO_3$ are subjected to a compressive biaxial in-plane strain of 0.9%. All layers were doped with Sm^{+3} (~1%). The Sm^{+3} doping in the $EuTiO_3$ capping layers facilitates electrical contact to the $SrTiO_3$. The carrier densities in the films are governed by the Sm dopant concentration. It has been previously found that the superconducting characteristics are unaffected by whether La^{+3} or Sm^{+3} is employed as a dopant in $SrTiO_3$ [53,57]. For comparison, doped, uncapped $SrTiO_3$ films with thicknesses of 70 nm, 40 nm, and 10 nm were grown on LSAT substrates and also investigated.

Figure 4.6 shows typical RHEED images taken after the growth of the $SrTiO_3$ layer (upper panel) and the $EuTiO_3$ layer (lower panel). Half-order surface reconstruction in the <1 0 0> azimuth appeared in both the $SrTiO_3$ layer and the $EuTiO_3$ layer. The RHEED patterns of the heterostructure reproduce the results of the calibration growth as shown previously. Notably, the RHEED patterns of the second $EuTiO_3$ layer are the same as that of $EuTiO_3$ layer grown on LSAT. The high-quality growth of the heterostructures was also examined by XRD (Figure 4.7). 002 film reflections detected. Any difference in the out-of-plane lattice parameters of the $SrTiO_3$ films and the $EuTiO_3$ films cannot be distinguished by XRD. The lattice parameter of samples A, B, and C were 3.932, 3.931, and 3.928 Å, respectively. These values are very close

to the expected lattice parameter of fully strained films. The 002 film reflections show thickness fringes, which is evidence of smooth film surfaces.

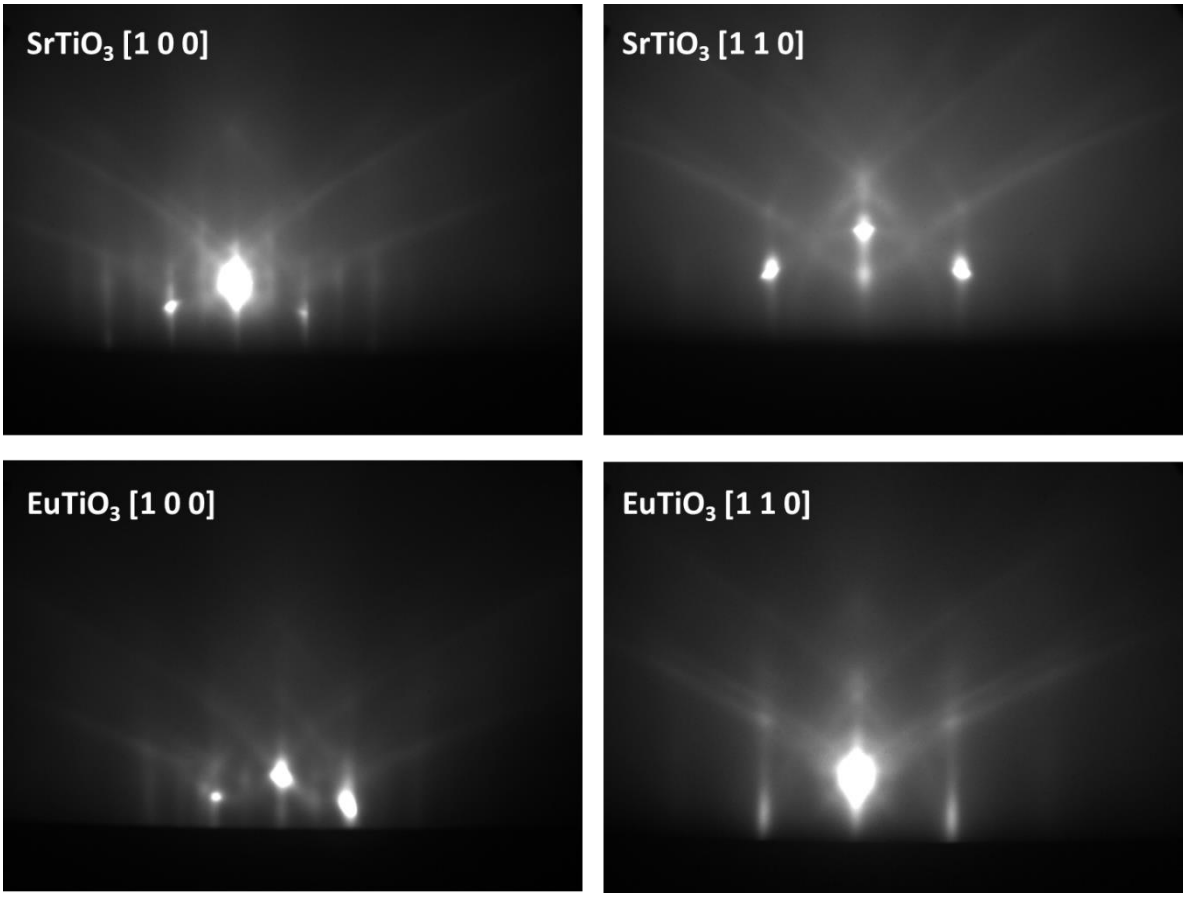

Figure 4.6 Post-growth RHEED images of typical $EuTiO_3$/ $SrTiO_3$ films along the [100] and [110] azimuths. Upper panel (lower panel) show the RHEED images after the growth of $SrTiO_3$ ($EuTiO_3$) layer.

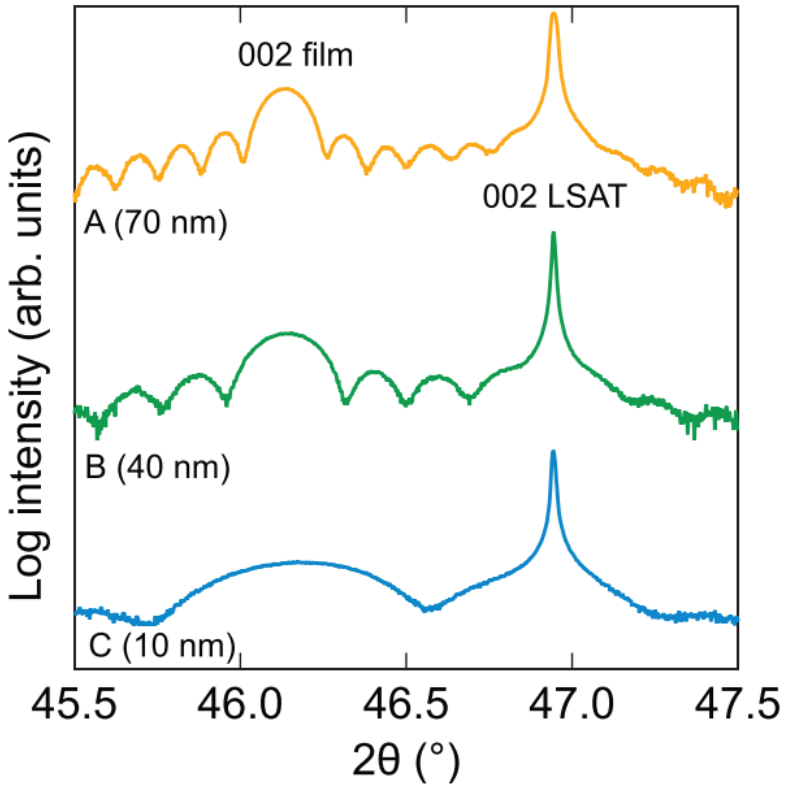

Figure 4.7 XRD patterns near the 002 films reflection of $EuTiO_3/SrTiO_3$ heterostructures on LSAT substrates. The thickness of the $EuTiO_3$ layer is ~ 10 nm for all samples. Reproduced from [58], with the permission of AIP Publishing

4.5 Electrical Properties of $EuTiO_3/SrTiO_3$ Heterostructures

The sheet resistance and carrier density of the heterostructures were studied in van der Pauw geometry. Ti/Au (50nm/250nm) edge metal contacts of the van der Pauw structure were deposited using an electron beam evaporator with an aluminum foil shadow mask. Hall carrier density (sheet carrier density) was determined using a Quantum Design Dynacool system. n_{3D} values were obtained by dividing the sheet carrier density by the total thickness of the films.

Figure 4.8 shows the sheet resistances of films A-C as a function of temperature from 300 K to 2 K. The sheet resistances of all the films show metallic behavior. Additionally, they decrease with increasing $SrTiO_3$ film thickness at around room temperature, which reflects parallel conduction in both $EuTiO_3$ and $SrTiO_3$. Figure 4.9 shows the sheet resistance values between 12 K to 2 K. The sheet resistances begin to rise around 6.5–7 K, followed by a sharp drop at the Neel temperature. This behavior is known as a unique characteristic of $EuTiO_3$ because of the strong spin fluctuation scattering of the conducting electrons by the localized Eu spins [104,105]. The results show the contribution of the $EuTiO_3$ to the measured resistance.

Figure 4.10 shows n_{3D} as a function of temperature. The estimated n_{3D} values at 300 K were 9×10^{19} cm^{-3}, 6×10^{19} cm^{-3}, and 9×10^{19} cm^{-3} for films A–C, respectively. Films A and B show a small reduction in n_{3D}. The n_{3D} difference between 300 K and 2 K is ~30%. The n_{3D} values start to decrease at ~100 K. The reduction is caused by ferroelectric transition where free carriers screen dipolar fields of ferroelectric polarization [15,106].

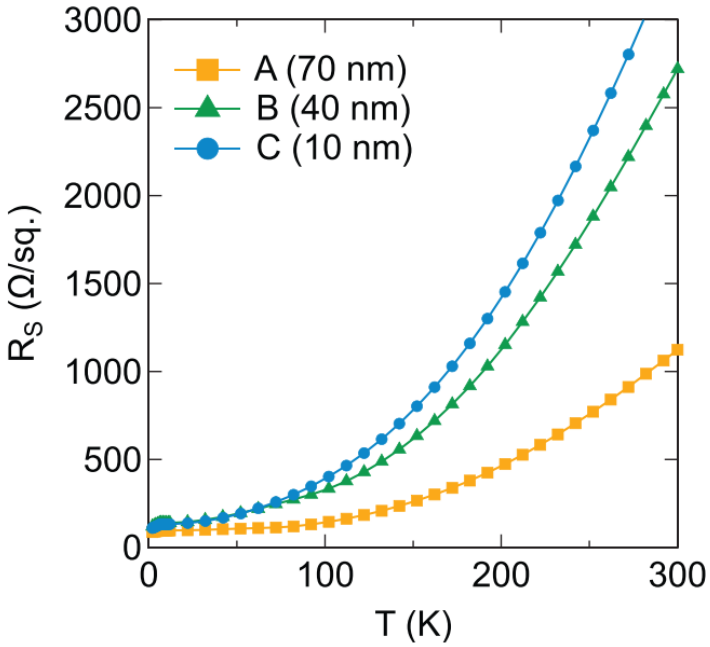

Figure 4.8 Sheet resistance of films A-C as a function of temperature between 300 K to 2 K. Reproduced from [58], with the permission of AIP Publishing.

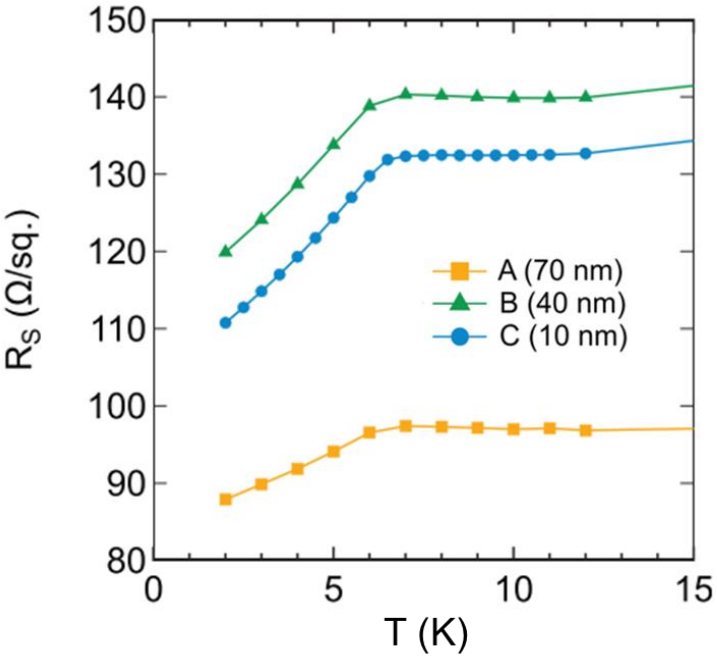

Figure 4.9 Sheet resistance of films A-C as a function of temperature between 12 K to 2 K. Adapted from [58], with the permission of AIP Publishing.

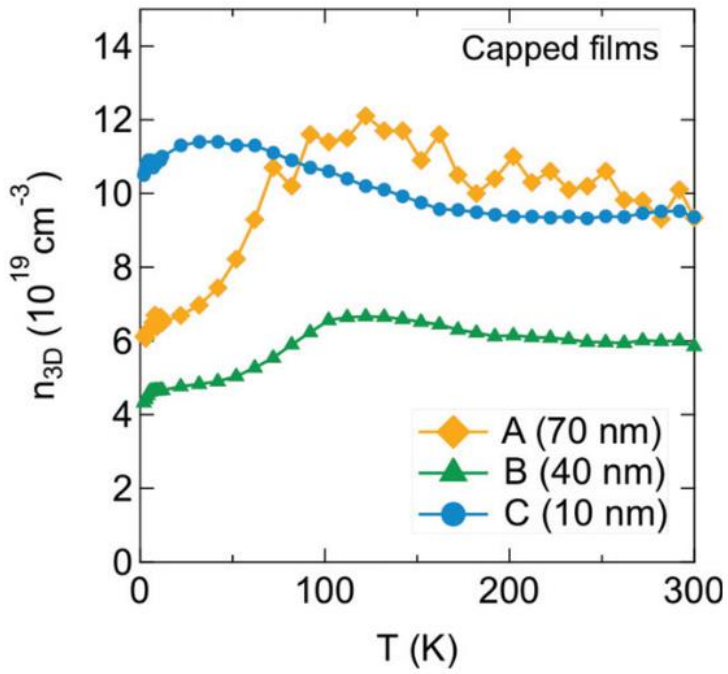

Figure 4.10 Carrier density (n_{3D}) as a function of temperature (T) for samples A, B, and C between 300K and 2 K. Adapted from [58], with the permission of AIP Publishing

In contrast, film C does not undergo carrier depletion and even shows a slight upturn in carrier density at low temperatures. Compared to films A and B, it appears that film C does not become ferroelectric because of the lack of the carrier density reduction at ~100K. However, further investigation is necessary. A slight increase in carrier density has been observed in $SrTiO_3$ quantum wells previously [107].

We can compare the electric properties of the capped films with those without uncapped $SrTiO_3$ films. Figure 4.11 shows sheet resistance of uncapped films. Unlike the capped films, the uncapped films are characterized as strong upturns in sheet resistance at low temperatures. In the case of the 10-nm-thick film, insulating behavior takes place even at room temperature, which reflects severe carrier depletion in thinner $SrTiO_3$ films. Therefore, this result demonstrates that the 10-nm-thick $EuTiO_3$ capping layer is effective to prevent $SrTiO_3$ thin films from metal to insulator transition.

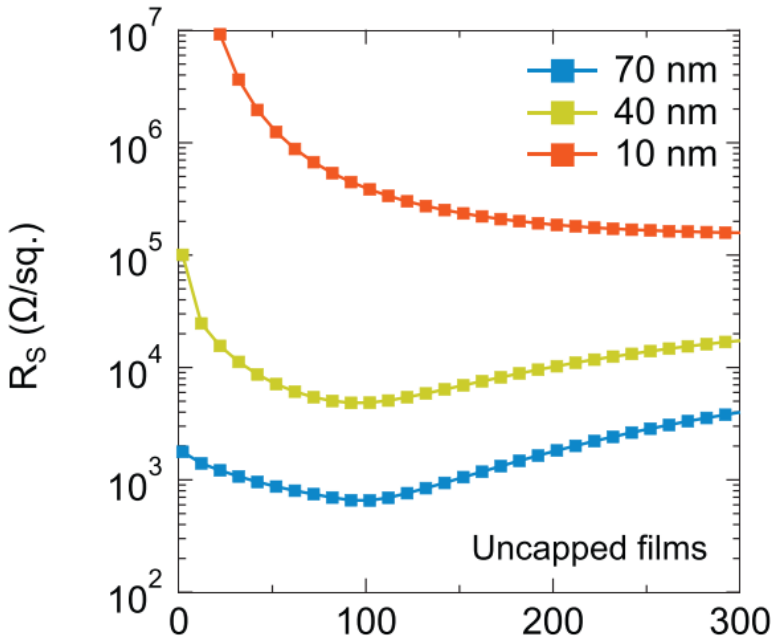

Figure 4.11 Sheet resistance as a function of temperature (T) for uncapped $SrTiO_3$ films between 300 K and 2 K. Adapted from [58], with the permission of AIP Publishing

Figure 4.12 shows n_{3D} of the uncapped films as a function of temperature. As shown in figure 4.11, The 10-nm- thick uncapped film is already insulating at room temperature. As a result, it was impossible to estimate its carrier [108]. Unlike the small reduction in the capped films, the uncapped films undergo large carrier depletion around 70 ~ 80% between 300 K and 2 K. Thus, the comparison demonstrates that $EuTiO_3$ capping layers reduce the surface carrier depletion that commonly plagues $SrTiO_3$ air-exposed surfaces.

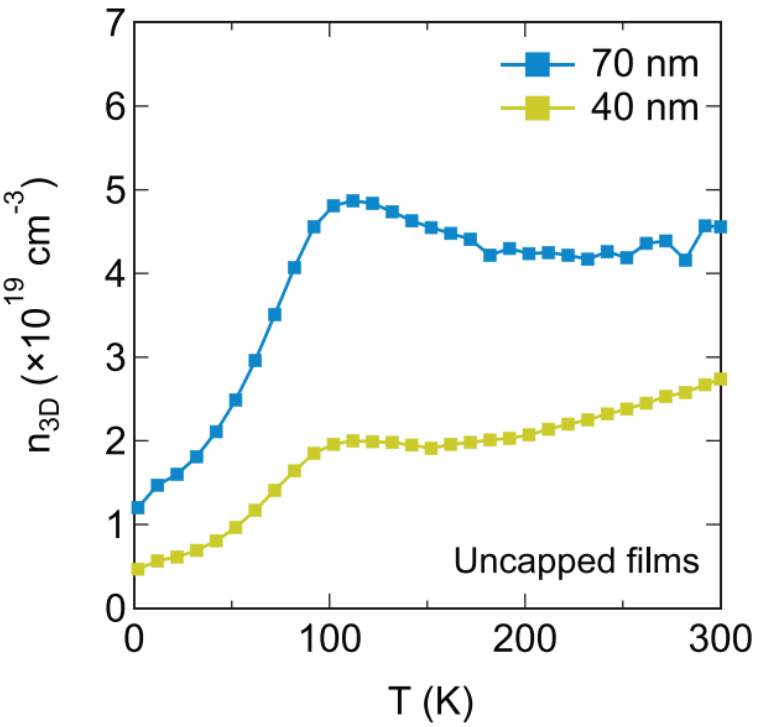

Figure 4.12 Carrier density (n_{3D}) as a function of temperature (T) for uncapped $SrTiO_3$ films between 300K and 2 K. Adapted from [58], with the permission of AIP Publishing

4.6 Thickness Dependence of Superconductivity in $EuTiO_3/SrTiO_3$ Heterostructures

Longitudinal resistances of the capped films were measured below 1 K using a dilution refrigerator (Oxford Triton) and lock-in amplifiers. The superconductivity was measured in either Hall bar geometry (film A) or van der Pauw geometry (films B and C). Figure 4.13 shows the longitudinal resistance (R) normalized to the normal resistance (R_n) below 1 K where R_n is the longitudinal resistance measured at 1 K. Films A and B become superconducting. The superconducting transition temperature (T_c) was defined as the temperature where R/R_n equals 0.05. The T_cs of films A and B are 420 mK and 320 mK, respectively. Although their superconducting transitions are sharp like thicker (~180 nm) uncapped $SrTiO_3$ films, the T_c is lower, despite the fact that their carrier densities ($6\sim9 \times 10^{19} cm^{-3}$) are close to the center of the superconducting dome [15]. Compared to unstrained bulk $SrTiO_3$ with similar carrier densities [3], only film A has somewhat enhanced T_c, while the T_c of film B is not enhanced. Moreover, film C, the thinnest film, is no longer superconducting. Thick strained, uncapped $SrTiO_3$ films (~180 nm) exhibit T_c values around 600 mK at similar carrier densities [15,57]. In particular, it appears that T_c is lowered progressively as the $SrTiO_3$ film thickness decreases.

Superconductivity in strained uncapped $SrTiO_3$ films was also investigated for comparison. 60-nm-thick uncapped $SrTiO_3$ thin film is superconducting with its T_c of ~400 mK which is similar to that of the capped 70nm film (film A), while the thinner uncapped film (40 nm) did not become superconducting. The result of uncapped 40 nm film is matched with a strong upturn in R_s and carrier depletion seen in Figures 4.11 and 4.12. The film can have

considerably reduced effective doped region. Overall, the results reveal a consistent suppression of T_C as the thickness of $SrTiO_3$ is decreased.

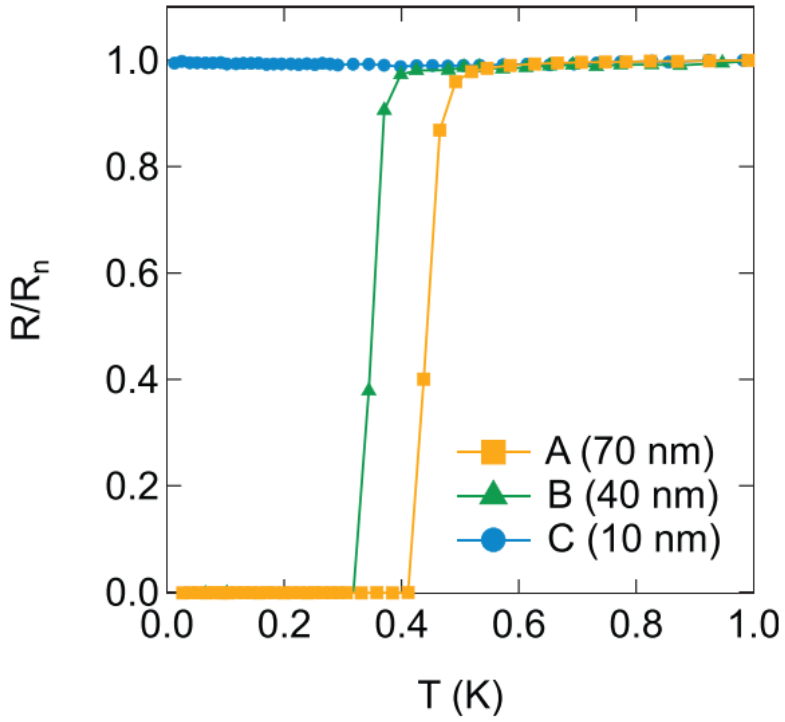

Figure 4.13 Normalized resistance of capped films A, B, and C as a function of temperature near the superconducting transition. Reprinted from [58], with the permission of AIP Publishing

4.7 Dependence on $EuTiO_3$ Capping Layer Thickness

A strained $SrTiO_3$ film with a thicker $EuTiO_3$ capping layer (~ 20 nm) was grown to investigate the effect of $EuTiO_3$ capping layer thickness on superconductivity in $SrTiO_3$ films. $SrTiO_3$ film thickness was fixed to ~70 nm, the same as that of film A. Thus, the new film was denoted as film A′.

Film A′ was characterized in the same methods in the previous sections and compared with film A. Figure 4.14 (a) shows out-of-plane XRD scans around 002 film reflections. Compared to film A, the 002 reflection of film A′ is still well-defined and symmetric without no indication of partial relaxation. Film A′ is fully strained despite its larger total film thickness than film A. The risk of partial strain relaxation increases with total film thickness. Slightly shorter intervals of thickness fringes of film A′ reflects an increase in the total film thickness of film A′ compared to film A.

Figure 4.14 (b) shows carrier densities (n_{3D}) of films A and A′ as a function of temperature. Film A′ was slightly more doped than film A. Room temperature n_{3D} of film A′ (1.1×10^{20} cm^{-3}) was higher than that of film A (9×10^{19} cm^{-3}). Aside from the initial carrier density difference, the dependence of n_{3D} on temperature for film A′ is similar to film A. n_{3D} of film A′ begins to drop at ~ 100 K which is a sign of ferroelectric transition in the $SrTiO_3$ layer. The reduction in n_{3D} of film A′ between 300 K and 2 K is ~20% a little bit less than that of film A. The surface depletion layer width is inversely proportional to the square root of n_{3D}, and ferroelectricity is degraded with an increasing number of free carriers.

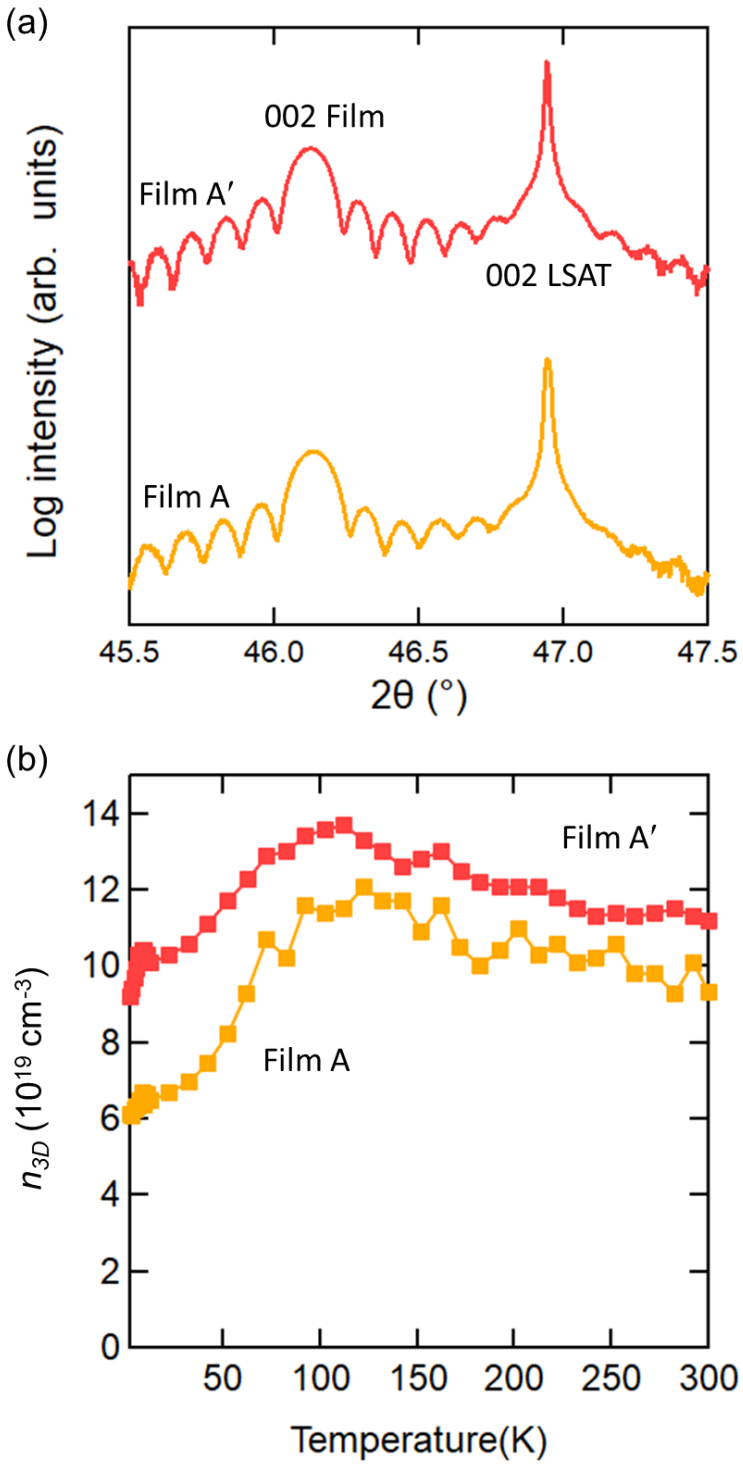

Figure 4.14 (a) out-of-plane XRD scans around 002 reflections of films A and A′. (b) carrier densities as a function of temperature.

Figure 4.15 shows longitudinal resistances of films A and A′ below 1 K. The resistance was measured in Hall bar devices. Film A′ becomes superconducting with T_c of ~ 360 mK slightly less than the T_c of film A (~ 420 mK). It is confirmed that both ~10 nm and ~20 nm $EuTiO_3$ capping layers effectively protect $SrTiO_3$ films from strong surface carrier depletion.

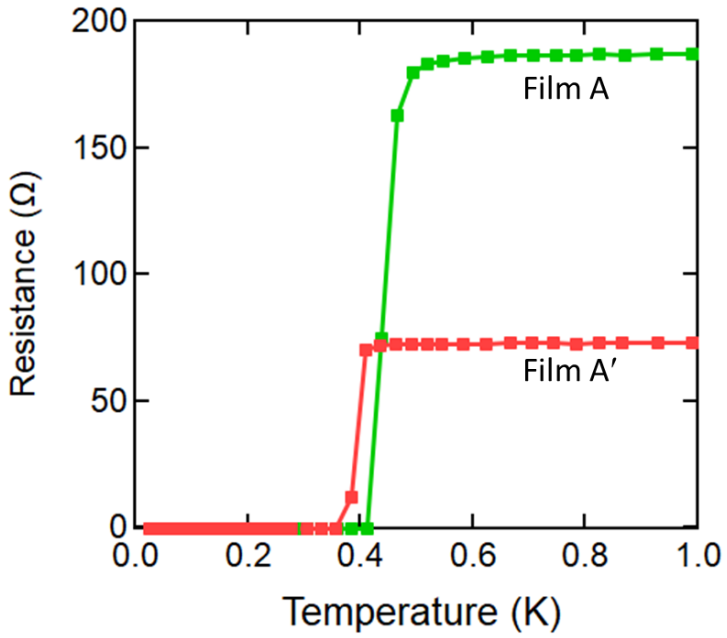

Figure 4.15 Longitudinal resistance of films A and A′ below 1K

4.8 Multilayer $EuTiO_3/SrTiO_3$ Heterostructure

Further superconductivity study was performed in a multilayered $EuTiO_3/SrTiO_3$ heterostructure. The original purpose of this study was to explore possible magnetically coupled superconductivity in $SrTiO_3$ films by means of $EuTiO_3$ layers. While the magnetic ground state of $EuTiO_3$ below T_n is antiferromagnetic, its magnetic state can be varied from antiferromagnetic to spin-flop to ferromagnetic under magnetic fields [109].

To induce strong magnetic coupling between the multilayer, the shorter interdistance between the $EuTiO_3$ layers gives rise to the stronger magnetic interaction between them. However, in the previous section, it turned out that the $EuTiO_3$ capped 10 nm-thick $SrTiO_3$ film does not become superconducting. Thus, the spacing between the $EuTiO_3$ layers should be greater than 10 nm. Therefore, $(EuTiO_3/SrTiO_3)_2$ heterostructure was grown on a (001) LSAT substrate (Figure 4.16). The thickness of each layer was 20 nm, and all the layers were doped with Sm^{3+}.

Figure 4.16 Schematic structure of $(EuTiO_3/SrTiO_3)_2$ heterostructure grown on (001) LSAT substrate. The thickness of each film is 20nm.

Figure 4.17 shows out-of-plane XRD data of the $(EuTiO_3/SrTiO_3)_2$ heterostructure near 002 film peak. Even though four independent film growths were made, the 002 film peak is symmetric with well-defined thickness fringes. The out-of-plane lattice parameter is 3.930 Å which indicates that the four-layered heterostructure is fully strained. n_{3D} of this film is 1.1×10^{20} cm^{-3}.

Figure 4.18 shows the longitudinal resistance of the multilayer structure below 1 K. The multilayered film does not become superconducting. The n_{3D} of 1.1×10^{20} cm^{-3} should be in the superconducting dome in the case of thick strained thin film (~180 nm) [15,57]. Thus, the non-superconducting characteristic of the film is attributed to suppression by the $SrTiO_3$ film thickness (20 nm) being thinner than the presumable critical thickness for superconductivity.

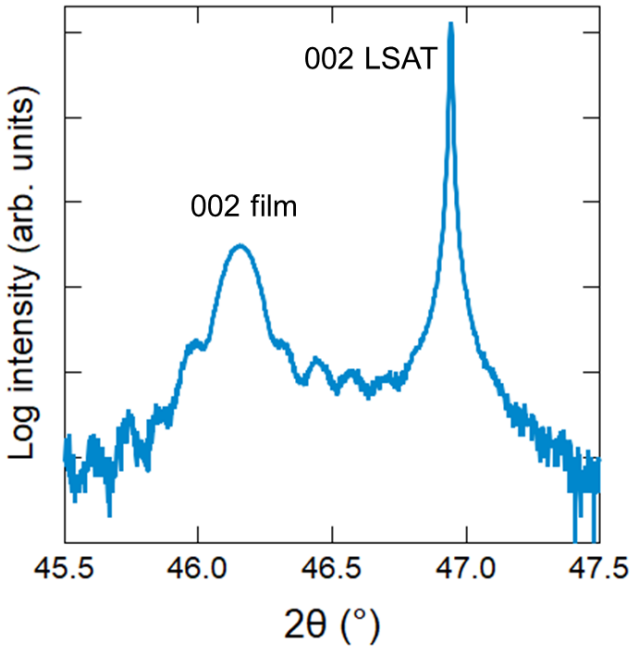

Figure 4.17 XRD patterns taken near the 002 film reflection of $(EuTiO_3/SrTiO_3)_2$ heterostructure

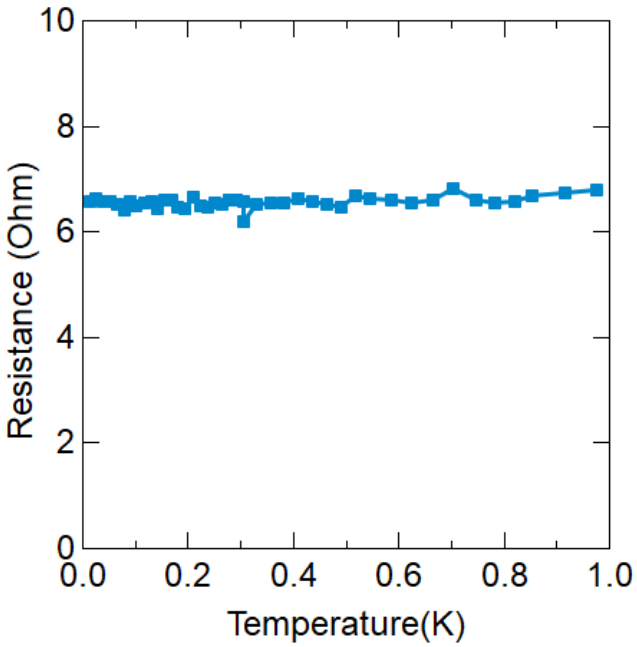

Figure 4.18 Longitudinal resistance of $(EuTiO_3/SrTiO_3)_2$ heterostructure below 1 K

4.9 Discussion and Conclusion

In summary, the data shows that $EuTiO_3$ capping layers can mitigate the surface carrier depletion, which is seen for uncapped, air-exposed $SrTiO_3$ films. However, the superconducting T_c for the capped thin films is lower than that of uncapped thick films. In addition, the T_c drops with decreasing $SrTiO_3$ film thickness, and the superconductivity is suppressed with an $SrTiO_3$ film thickness less than 40 nm.

First, the effect of the $EuTiO_3$ capping layers on the T_c of the $SrTiO_3$ films is considered. In view of $EuTiO_3$'s magnetism, doped, strained $EuTiO_3$ films are G-type antiferromagnetic [109]. Therefore, it can be assumed that the magnetic influence of the $EuTiO_3$ layers is negligible. Nevertheless, a reduction in T_c still is expected for superconductor/ normal metal bilayer system. In the bilayer system, the superconducting pair correlations extend into the normal metal ($EuTiO_3$ in our case) [110,111]. The suppression of T_c as observed in the 10 nm bilayer film and the 20 nm $SrTiO_3$ layers in the multilayered heterostructure suggests that the coherence lengths in the superconductor and the normal layers are greater than the thicknesses of these layers [110]. The result of the $EuTiO_3$ layer thickness study might let us conclude that a thicker $EuTiO_3$ layer gives rise to the reduction in T_c of superconductivity in $SrTiO_3$, but more data points are required because the T_c variation near the carrier density range ($\sim 10^{20} cm^{-3}$) is larger than 60 mK (see figure 3.3). The theory of superconductor/normal metal bilayer predicts that the T_c drops with the thickness of the normal layer, but the reduction is saturated at a certain critical thickness [110]. Regardless, the study demonstrates that both 10 nm and 20 nm $EuTiO_3$ are appropriate capping layers for the superconductivity study.

Second, the possibility of free electron transfer from $SrTiO_3$ to $EuTiO_3$ also needs to be considered. According to density functional calculations, the conduction band edge of $EuTiO_3$ is higher than that of $SrTiO_3$ by 0.4 eV [112,113]. Therefore, charge transfer from $SrTiO_3$ to $EuTiO_3$ is not predicted, and $EuTiO_3$ should not deplete $SrTiO_3$. Lastly, (incipient) ferroelectricity in strained $SrTiO_3$ films could play a crucial role in the superconductivity [114], and ferroelectric characteristics could be modified in thinner films (20 nm and 10 nm). Further studies were necessary to determine the contribution of each scenario.

Chapter 5

Critical Thicknesses for Superconductivity and Ferroelectricity in Strained $SrTiO_3$ Thin Films

5.1 Introduction

One of the unusual characteristics of superconductivity in $SrTiO_3$ is its emergence in the noncentrosymmetric polar phase [15,36,45,115], which offers opportunities for the realization of polar superconductor-specific phenomena [54,116–118]. Also, theoretical discussions regarding ferroelectric fluctuations and/or a soft mode mediated superconductivity have been made [47,119–121]. Nevertheless, there is no consensus on how $SrTiO_3$ becomes superconducting [4]. For compressively strained $SrTiO_3$ films, it has been already shown that their superconductivity emerges in a polar phase [15,36]. Although these results are difficult to reconcile with the ferroelectric fluctuation or soft mode-based theories, it appears that there are close connections between superconductivity and ferroelectricity in the $SrTiO_3$ films. First, the superconducting T_c is enhanced in samples that undergo a ferroelectric transition [15,115,122]. Second, ferroelectricity and superconductivity disappear at similar carrier concentrations on the overdoped side of the superconducting dome [36]. Third, the superconducting T_c seems to scale with the length scale of polar order [114].

The putative connection between the two phenomena can be further studied by investigating critical thicknesses for superconductivity and ferroelectricity. In the previous chapter, the $EuTiO_3$ capped 10 nm $SrTiO_3$ film did not become superconducting and had no sign of a ferroelectric transition in the carrier density profile, which gives a clue about the relationship between the two critical thicknesses. Ferroelectric perovskite thin films generally exhibit a critical thickness below which ferroelectricity is suppressed by depolarization fields [123–126]. Superconducting T_c can be also decreased with film thickness [127], though

the reason for the reduction in T_c varies and two-dimensional superconductors can certainly exist.

This chapter reports on the thickness dependence of superconductivity and ferroelectricity in doped, compressively strained $SrTiO_3$ thin films. It is observed that both superconductivity and ferroelectricity are simultaneously suppressed in thin films. This observation supports a connection between the two phenomena.

5.2 Methods

Compressively strained, Sm-doped $SrTiO_3$ films with different thicknesses (70 nm, 40 nm, 25 nm, and 10 nm) were grown on LSAT substrates by hybrid molecular beam epitaxy as introduced in Chapter 2. A 10 nm thick Sm-doped $EuTiO_3$ capping layer was deposited to mitigate surface carrier depletion [58]. Here, the $EuTiO_3$-capped $SrTiO_3$ films with thickness of X nm are denoted as ESX to avoid confusion between sample names used in previous chapters. For example, ES70 stands for the capped 70 nm thick $SrTiO_3$ film. Their Hall carrier densities (n_{3D}) were determined in van der Pauw geometry using a Quantum Design Dynacool System. At room temperature, n_{3D} corresponded to 9×10^{19} cm^{-3} (ES70), 6×10^{19} cm^{-3} (ES40), 1.2×10^{20} cm^{-3} (ES25), and 9×10^{19} cm^{-3} (ES10), close to the carrier densities for the maximum in T_c. ES70 and ES40 appeared as films A and B in Chapter 4, respectively. In addition, 25 nm and 10 nm thick $SrTiO_3$ films without capping layers (S25 and S10) were grown for comparison. XRD, superconducting T_c, and upper critical magnetic field (H_{c2}) were measured using the same methods mentioned in previous chapters.

Optical second harmonic generation (SHG) experiments were performed to investigate ferroelectric order in the samples. Ultrafast laser pulses with 800 nm center wavelength, 40 fs duration, and 10 kHz repetition rate were focused to a spot size of 30 μm, as described in ref. [36]. The optical SHG measurements were done by Ryan Russell in the Harter group at UCSB.

5.3 Film Growth and Superconducting Properties

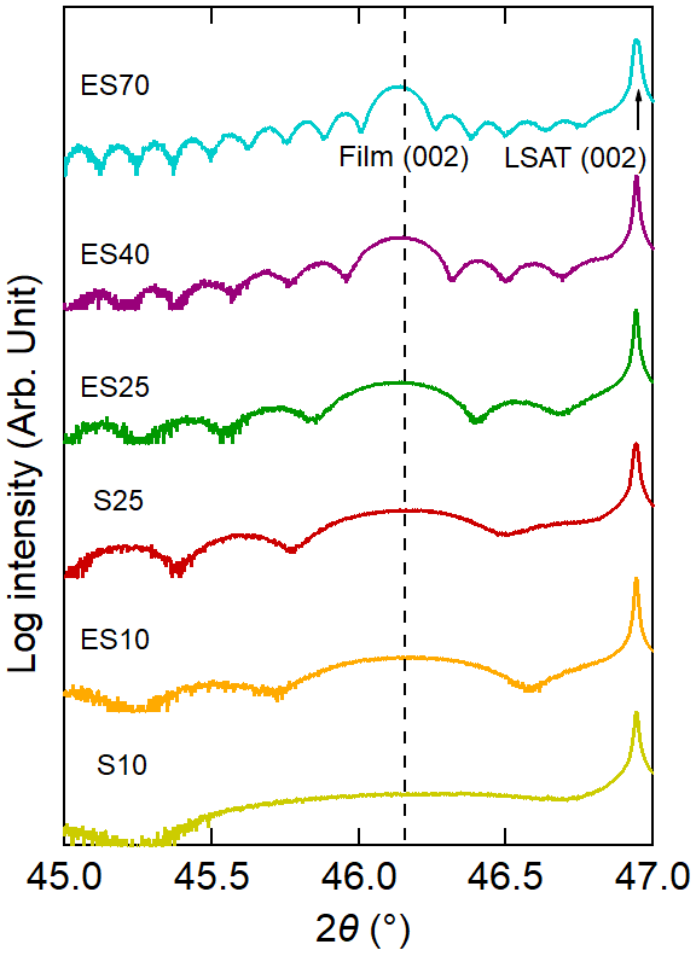

Figure 5.1. Out-of-plane XRD scan around 002 film peak. The 2θ position for out-of-plane lattice parameter of fully strained film is indicated by the dashed line. Adapted from [59], with the permission of AIP Publishing.

Figure 5.1 shows out-of-plane XRD scans around 002 film peak for all films studied in this chapter. The dashed line indicates the 2θ angle corresponding to the lattice parameter of fully strained films. The out-of-plane lattice parameters of all the films were 3.930 ± 0.002Å. These values are close to the known lattice parameter of coherently, compressively strained film and demonstrates that the films are strained and stoichiometric. Compressively strained $SrTiO_3$ becomes ferroelectric along the out-of-plane film direction with single

domain [36,128]. Clear thickness fringes show that smooth surface and that the films are not relaxed.

Figure 5.2 shows normalized resistances of the capped films (ES10 through ES70). As clearly seen in the figure, the two thicker films (ES70 and ES40) exhibit a superconducting transition.

The extracted values for T_c of ES70 and ES40 are 410 mK and 320 mK, respectively. However, the two thinner capped films (ES25 and ES10) never become superconducting down to the base temperature.

Figures 5.3 and 5.4 show normalized resistance of ES70 and ES40 as a function of magnetic fields. The extracted in-plane and out-of-plane H_{c2} of ES70 are 1.2 T and 0.77T, respectively. In the case of ES40, the in-plane and out-of-plane H_{c2} are 2.7 T and 1.0 T, respectively. In-plane H_{c2} values of both samples are higher than their out-of-plane H_{c2}, which is typical of thin film superconductors [57]. In thin film geometry, in-plane H_{c2} is enhanced due to the suppression of orbital pair breaking [83].

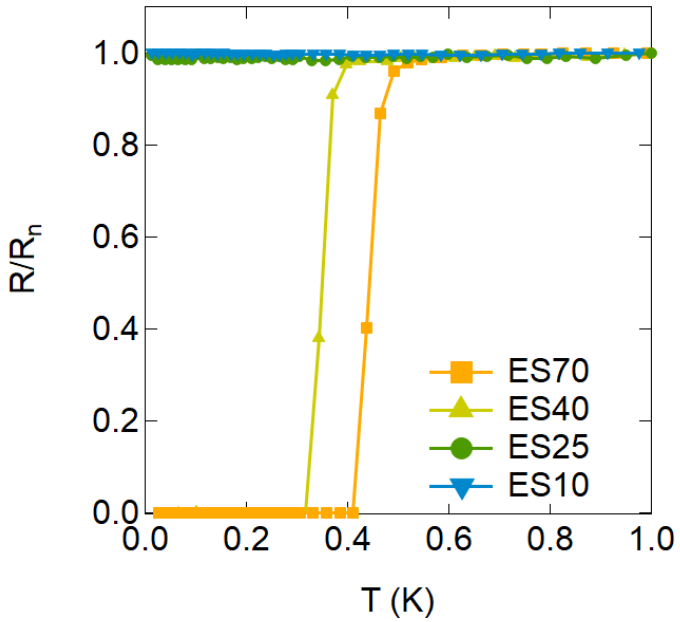

Figure 5.2. Normalized resistance as a function of temperature for capped films. Adapted from [59], with the permission of AIP Publishing.

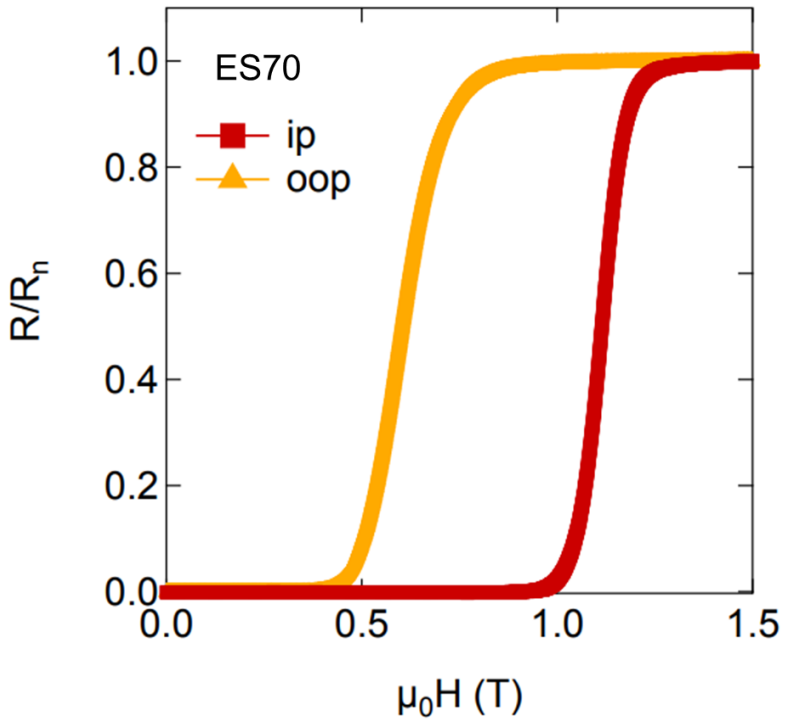

Figure 5.3. Normalized resistance as a function of in-plane (ip) and out-of-plane (oop) magnetic fields for ES70. Adapted from [59], with the permission of AIP Publishing.

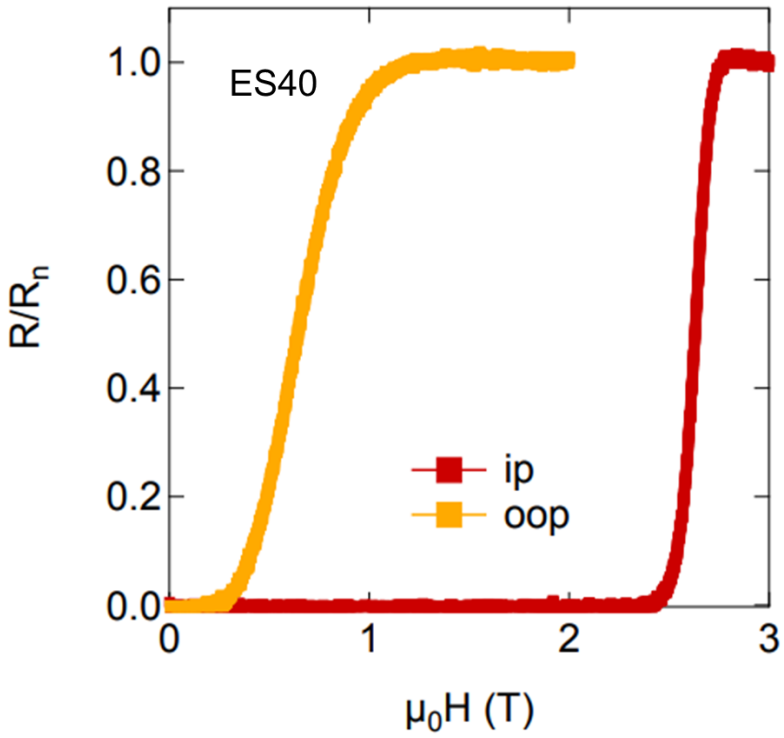

Figure 5.4. Normalized resistance as a function of in-plane (ip) and out-of-plane (oop) magnetic fields for ES40. Adapted from [59], with the permission of AIP Publishing.

5.4 Thickness Dependent Ferroelectricity in Strained $SrTiO_3$ films

The ferroelectricity of all the samples was investigated using optical SHG. Optical SHG can detect inversion symmetry breaking so it is useful to measure the ferroelectric transition of conducting $SrTiO_3$ thin films for which conventional polarization-electric field measurement does not work. Each data point shown in the optical SHG figures in this section was obtained by taking an average of multiple measurements while the temperature is changed. The majority of noise arises from fluctuations of the laser power, and the error bars show root mean square errors from linear fits to the data from films that did not undergo a ferroelectric transition.

Figure 5.5 (a) shows optical SHG intensities for the two thicker superconducting samples (ES70 and ES40) as a function of temperature. ES70 and ES40 undergo a ferroelectric transition at ~ 100 K. The ferroelectric transition is characterized by non-linear enhancement in SHG intensity. Figure 5.5 (b) shows the SHG intensities for the non-superconducting thinner samples (ES25 and ES10). The intensity trend is linear, and they do not become ferroelectric. Figure 5.5 (b) also shows the results of uncapped films (S25 and S10) to exclude the possibility of concealing ferroelectric transition by the $EuTiO_3$ capping layer. We note, however, that uncapped films are depleted of carriers, which in turn may affect the stability of the ferroelectric phase [129]. Like the two thinner capped films, the two thinner uncapped films do not become ferroelectric. For S25, there is a hump around 70 K, but the intensity trend gets back to linear below 50 K. All films show a nonzero SHG intensity above the ferroelectric transition temperature, which could be due to inversion symmetry breaking at

interfaces or surfaces, polar nanodomains, and higher-order terms independent of inversion symmetry breaking [36,114,130].

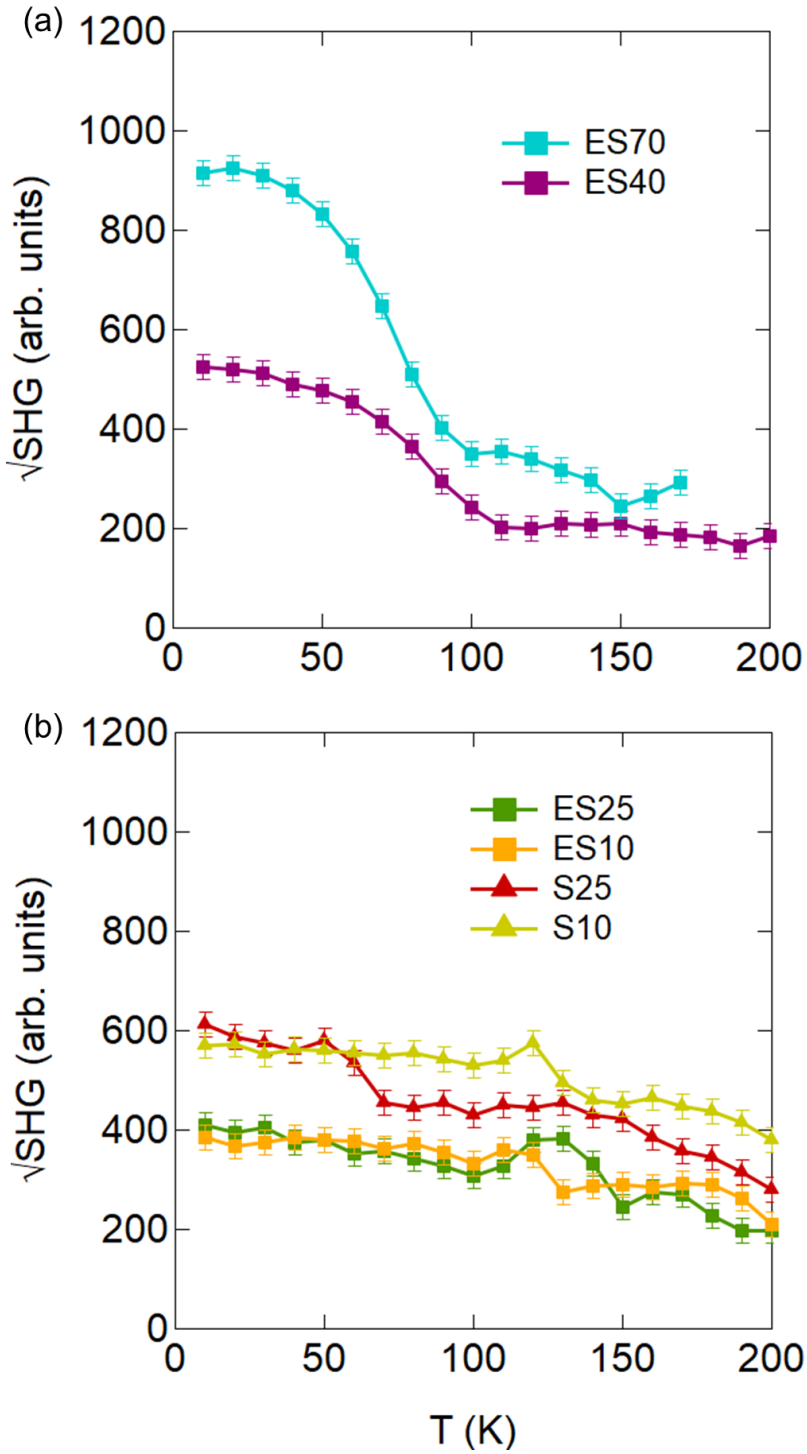

Figure 5.5 Optical second harmonic generation intensity for (a) superconducting sample group and (b) non-superconducting sample group, and uncapped samples as a function of temperature. Adapted from [59], with the permission of AIP Publishing.

5.5 Discussion and Conclusion

The apparent critical thickness for ferroelectricity is considerably large between 25 nm and 40 nm, compared to other undoped ferroelectric materials. Their critical thicknesses are usually within a few nm [123–126]. In addition, undoped strained $SrTiO_3$ thin films with a thickness of 20 nm become ferroelectric [130]. The large critical thickness is explained by the combination of free carriers and uncompensated surface bound charges on the oxide surface without conducting electrodes of which free carriers compensate for the bound charges, resulting in a reduction in the depolarization field. Also, $SrTiO_3$ itself could be considered a weak ferroelectric because external perturbation (ex. alloying or strain) is needed for $SrTiO_3$ to get ferroelectric, unlike $BaTiO_3$ and $PbTiO_3$.

Moreover, considering earlier discoveries of superconductivity in quasi-two-dimensional electron systems in $SrTiO_3$ [131,132], the absence of superconductivity as thick as 25 nm is even more unexpected. There are a few possible explanations. First, carrier depletion is not expected in the capped films because all samples have similar carrier density and it was demonstrated that free carriers were preserved in a thinner capped film in the previous chapter. The normal resistance of the samples studied here ranges from 20 Ω ~ 200 Ω. This range of resistances is well below the resistance range where localization phenomena become important [133].

The key finding from this study is that superconductivity and ferroelectricity are suppressed at around the same thickness. Although this observation might be a coincidence, the meaning of this result is discussed in relation to the connection between superconductivity and ferroelectricity in $SrTiO_3$. This observation implies that superconductivity in $SrTiO_3$ is

closely connected to the presence of a polar phase, which is in agreement with prior results. For example, our previous results have indicated that a polar phase is associated with an enhancement of T_c in strained $SrTiO_3$ films [36,114]. In addition, a very recent study shows greater enhancement of T_c of polar (Sr, Ba)TiO_3 and (Sr, Ca)TiO_3 alloys inside polar regions than in the vicinity of ferroelectric quantum critical point [49].

Overall, recent experiment results including our data hint that the role of spin-orbit coupling in the superconductivity, because it is present in the polar phase due to inversion symmetry breaking, but is absent in films that do not become ferroelectric. Previous studies have underlined the significance of (Rashba) spin-orbit coupling in the superconductivity of quasi-two-dimensional electron gas [83,134]. Taken together, all of these results should motivate further studies into the role of spin-orbit coupling in the superconductivity of $SrTiO_3$.

Chapter 6

Summary and Future Directions

6.1 Summary of Dissertation

In Chapter 1, the physical properties of $SrTiO_3$, the material of interest in this dissertation, were briefly reviewed, chiefly its electronic, ferroelectric, and superconducting properties. The unusual characteristics of the superconductivity of $SrTiO_3$ were also introduced, such as its superconductivity at very low carrier densities and exotic connection between ferroelectricity and superconductivity, as the superconducting T_c is enhanced inside the ferroelectric phase.

In Chapter 2, we introduced the general methodologies used in the research for this dissertation. High-quality, strained $SrTiO_3$ thin films were grown using hybrid MBE. Compared to conventional MBE, the hybrid MBE, which uses a metalorganic source (TTIP), allows for high vapor pressure and a wider growth window. The film quality was investigated by in-situ RHEED and XRD, and electrical properties like sheet resistance and carrier density were measured in a van der Pauw geometry or a Hall bar device using a Quantum Design Dynacool System.

In Chapter 3, the superconducting properties in doped, strained $SrTiO_3$ films were studied. $SrTiO_3$ films with various carrier densities were grown for this study, and the maximum superconducting T_c was around ~600 mK. The in-plane upper critical fields of most samples with their carrier density between 5×10^{19} cm^{-3} and 9×10^{19} cm^{-3} were larger than Pauli limiting field. Since Pauli limiting field is the magnetic field that starts to break conventional spin-singlet Cooper pairs, violation of this limit has been often used as an indicator of unconventional superconductivity. In addition, second harmonic resistances, which may

indicate mixed-parity superconductivity, were measured in some of the samples. The common feature between the samples was partial strain relaxation.

In Chapter 4, electric and superconductivity in thinner $SrTiO_3$ nanofilms were studied. The film thicknesses of the samples used in the previous chapter were 160 nm ~ 180 nm to avoid large carrier depletion by strong surface depletion in $SrTiO_3$ thin films [82]. $EuTiO_3$ was introduced as a capping material. $EuTiO_3$ has a lower dielectric constant at low temperatures [100], so the surface depletion region width is narrow in $EuTiO_3$. We showed that a 10-nm-thick $EuTiO_3$ capping layer was effective at reducing surface depletion. $EuTiO_3$-capped $SrTiO_3$ films with various thicknesses (70 nm, 40 nm, and 10nm) exhibited metallic behaviors down to low temperatures. Also, the reduction in carrier density becomes less pronounced compared to uncapped films. Superconductivity could be measured in the capped 70 nm and 40 nm-thick $SrTiO_3$ films, proving that the $EuTiO_3$ capping layer is a successful strategy to get thin $SrTiO_3$ films superconducting. However, this work leaves an interesting question about the loss of superconductivity in the capped 10-nm-thick film despite the absence of carrier depletion.

In Chapter 5, the connection between ferroelectricity and superconductivity was further studied in strained $SrTiO_3$ thin films by reducing film thickness. Along with the earlier reports regarding the connection [15,36,114,115,122], the result of the capped 10-nm-thick $SrTiO_3$ films in chapter 4 motivated this work. The film was not only non-superconducting but also non-ferroelectric. To investigate the thickness-dependent relationship between the two phenomena, $EuTiO_3$-capped $SrTiO_3$ films with various thicknesses (70 nm, 40 nm, 25 nm, and 10 nm) were grown and analyzed. It was found that only the two thicker (70 nm and 40 nm) films became both ferroelectric and superconducting. However, the two thinner films

became neither ferroelectric nor superconducting. The ferroelectric transition was probed through optical SHG experiments, and the presence of $EuTiO_3$ capping layers did not change the conclusion of this work. A simultaneous suppression of superconductivity and ferroelectricity was observed at the same thickness (~ 25 nm). This work strengthens the putative link between the two phenomena, emphasizing the role of inversion symmetry breaking (spin-orbit coupling) in the superconductivity in $SrTiO_3$ films.

6.2 Further Growth Studies

We suggest future research directions based on the research findings in this dissertation. Currently, it has been challenging to create superconductivity in doped, strained $SrTiO_3$ films with thicknesses less than 40 nm as discussed in Chapters 4 and 5. Given our results, stronger driving forces for ferroelectricity could lead to superconductivity in thinner $SrTiO_3$ films. Since it is expected that ferroelectric T_c increases with the degree of in-plane strain [35,135], it looks promising that growing $EuTiO_3/SrTiO_3$ heterostructures on substrates of which lattice constant is smaller than LSAT (3.868Å) such as $LaAlO_3$ (3.879Å, pseudo-cubic). Moreover, (110) $DyScO_3$ substrates (3.944Å, pseudo-cubic [63]), give an in-plane a tensile strain (1%). It is known that tensile strained $SrTiO_3$ films grown on $DyScO_3$ undergo ferroelectric transition with in-plane polarization near room temperature [35], indicating a strong driving force by the tensile strain. Polarization leaves bound charges on the surface where the polarization vector meets. As a result, the depolarization field, one of the factors that increase ferroelectric critical thickness, of in-plane polarization should be much weaker. Thus, it is possible that $DyScO_3$ substrates result in much thinner critical thicknesses for ferroelectricity and superconductivity than LSAT substrates. The limitation of the growth of $SrTiO_3$ films on $DyScO_3$ substrates has been a low critical thickness for strain relaxation (~50 nm) [136]. While it is challenging to study superconductivity in uncapped 50-nm-thick films due to the strong surface carrier depletion, the $EuTiO_3$ capping layer beautifully settles the concern as extensively discussed in Chapter 4.

6.3 Superconductivity Diode Effect Measurement

A diode is a fundamental nonreciprocal electronic device, that has been a backbone of modern electronics. Electric current rectification by the diode effect provides essential elements for the basic operations of modern electronic devices. Conventional semiconductor devices based on p-n junction diodes have been developed constantly over the last few decades.

As discussed in Chapter 3, nonreciprocal transport is theoretically predicted in noncentrosymmetric superconductors under magnetic fields [80]. Though second harmonic resistances from some partially strained $SrTiO_3$ films could be observed [57], it is challenging to reproduce the same level of partial strain, and the origin of the second harmonic signal is still inconclusive. Measuring the difference between critical currents with respect to two opposite current directions can provide a clearer picture rather than the second harmonic resistance.

Direct observation of the superconducting diode effect by measuring asymmetric superconducting critical currents was first demonstrated in a Nb/V/Ta superlattice where inversion symmetry is artificially broken by the growth of the superlattice [137]. Strained, ferroelectric, superconducting $SrTiO_3$ films are still good candidates to investigate the superconducting diode effect due to their spontaneous inversion symmetric breaking. Film thickness and carrier densities can be further tuned for the study. In addition, $EuTiO_3/SrTiO_3$ heterostructures look also worth investigating. The doped $EuTiO_3$ layer is antiferromagnetic [138].

Bibliography

[1] A. Prakash and B. Jalan, *Molecular Beam Epitaxy for Oxide Electronics*, In Molecular Beam Epitaxy: Materials and Applications for Electronics and Optoelectronics. 423–452 (John Wiley & Sons Ltd, 2019)

[2] J. F. Schooley, W. R. Hosler, and M. L. Cohen, *Superconductivity in Semiconducting $SrTiO_3$*, Phys. Rev. Lett. **12**, 474 (1964).

[3] C. S. Koonce, M. L. Cohen, J. F. Schooley, W. R. Hosler, and E. R. Pfeiffer, *Superconducting Transition Temperatures of Semiconducting $SrTiO_3$*, Phys. Rev. **163**, 380 (1967).

[4] M. N. Gastiasoro, J. Ruhman, and R. M. Fernandes, *Superconductivity in Dilute $SrTiO_3$: A Review*, Ann. Phys. (Amsterdam). **417**, 168107 (2020).

[5] Y. Y. Pai, A. Tylan-Tyler, P. Irvin, and J. Levy, *Physics of $SrTiO_3$-Based Heterostructures and Nanostructures: A Review*, Rep. Prog. Phys. **81**, 036503 (2018).

[6] J. A. Sulpizio, S. Ilani, P. Irvin, and J. Levy, *Nanoscale Phenomena in Oxide Heterostructures*, Annu. Rev. Mater. Res. **44**, 117 (2014).

[7] D. G. Schlom, L. Q. Chen, C. J. Fennie, V. Gopalan, D. A. Muller, X. Pan, R. Ramesh, and R. Uecker, *Elastic Strain Engineering of Ferroic Oxides*, MRS Bull. **39**, 118 (2014).

[8] F. W. Lytle, *X-Ray Diffractometry of Low-Temperature Phase Transformations in Strontium Titanate*, J. Appl. Phys. **35**, 2212 (1964).

[9] P. A. Fleury, J. F. Scott, and J. M. Worlock, *Soft Phonon Modes and the 110°K Phase Transition in $SrTiO_3$*, Phys. Rev. Lett. **21**, 16 (1968).

[10] K. A. Müller, W. Berlinger, and F. Waldner, *Characteristic Structural Phase Transition in Perovskite-Type Compounds*, Phys. Rev. Lett. **21**, 814 (1968).

[11] K. van Benthem, C. Elsässer, and R. H. French, *Bulk Electronic Structure of $SrTiO_3$: Experiment and Theory*, J. Appl. Phys. **90**, 6156 (2001).

[12] T. Higuchi, T. Tsukamoto, N. Sata, M. Ishigame, Y. Tezuka, and S. Shin, *Electronic Structure of p-Type by Photoemission Spectroscopy*, Phys. Rev. B **57**, 6978 (1998).

[13] H. Suzuki, H. Bando, Y. Ootuka, I. H. Inoue, T. Yamamoto, K. Takahashi, and Y. Nishihara, *Superconductivity in Single-Crystalline $Sr_{1-x}La_xTiO_3$*, J. Phys. Soc. Japan **65**, 1529 (1996).

[14] J. Son, P. Moetakef, B. Jalan, O. Bierwagen, N. J. Wright, R. Engel-Herbert, and S. Stemmer, *Epitaxial $SrTiO_3$ Films with Electron Mobilities Exceeding 30,000 $cm^2 V^{-1}s^{-1}$*, Nat. Mater. **9**, 482 (2010).

[15] K. Ahadi, L. Galletti, Y. Li, S. Salmani-Rezaie, W. Wu, and S. Stemmer, *Enhancing Superconductivity in $SrTiO_3$ Films with Strain*, Sci. Adv. **5**, eaaw0120 (2019).

[16] Y. Ayino, J. Yue, T. Wang, B. Jalan, and V. S. Pribiag, *Effects of Paramagnetic Pair-Breaking and Spin-Orbital Coupling on Multi-Band Superconductivity*, J. Phys. Condens. Matter **32**, 38LT02 (2020).

[17] A. Leitner, C. T. Rogers, J. C. Price, D. A. Rudman, and D. R. Herman, *Pulsed Laser Deposition of Superconducting Nb-Doped Strontium Titanate Thin Films*, Appl. Phys. Lett. **72**, 3065 (1998).

[18] T. Zhao, H. Lu, F. Chen, S. Dai, G. Yang, and Z. Chen, *Highly Conductive Nb Doped $SrTiO_3$ Epitaxial Thin Films Grown by Laser Molecular Beam Epitaxy*, J. Cryst. Growth **212**, 451 (2000).

[19] X. Lin, Z. Zhu, B. Fauqué, and K. Behnia, *Fermi Surface of the Most Dilute Superconductor*, Phys. Rev. X **3**, 021002 (2013).

[20] D. Van Der Marel, J. L. M. Van Mechelen, and I. I. Mazin, *Common Fermi-Liquid Origin of T^2 Resistivity and Superconductivity in n-Type $SrTiO_3$*, Phys. Rev. B **84**, 205111 (2011).

[21] H. Uwe, R. Yoshizaki, T. Sakudo, A. Izumi, and T. Uzumaki, *Conduction Band Structure of $SrTiO_3$*, Jpn. J. Appl. Phys. **24**, 335 (1985).

[22] H. Uwe, T. Sakudo, and H. Yamaguchi, *Interband Electronic Raman Scattering in $SrTiO_3$*, Jpn. J. Appl. Phys. **24**, 519 (1985).

[23] K. A. Müller and H. Burkard, *$SrTiO_3$: An Intrinsic Quantum Paraelectric Below 4 K*, Phys. Rev. B **19**, 3593 (1979).

[24] W. Zhong and D. Vanderbilt, *Effect of Quantum Fluctuations on Structural Phase Transitions in $SrTiO_3$ and $BaTiO_3$*, Phys. Rev. B **53**, 5047 (1996).

[25] M. Itoh, R. Wang, Y. Inaguma, T. Yamaguchi, Y. J. Shan, and T. Nakamura, *Ferroelectricity Induced by Oxygen Isotope Exchange in Strontium Titanate Perovskite*, Phys. Rev. Lett. **82**, 3540 (1999).

[26] R. Wang and M. Itoh, *Suppression of the Quantum Fluctuation in ^{18}O-enriched Strontium Titanate*, Phys. Rev. B **64**, 174104 (2001).

[27] T. Mitsui and W. B. Westphal, *Dielectric and X-Ray Studies of $Ca_xBa_{1-x}TiO_3$ and $Ca_xSr_{1-x}TiO_3$*, Phys. Rev. **124**, 1354 (1961).

[28] J. G. Bednorz and K. A. Müller, *$Sr_{1-x}Ca_xTiO_3$: An XY Quantum Ferroelectric with Transition to Randomness*, Phys. Rev. Lett. **52**, 2289 (1984).

[29] V. Lemanov, E. Smirnova, P. Syrnikov, and E. Tarakanov, *Phase Transitions and*

Glasslike Behavior in $Sr_{1-x}Ba_xTiO_3$, Phys. Rev. B **54**, 3151 (1996).

[30] R. Wang, Y. Inaguma, and M. Itoh, *Dielectric Properties and Phase Transition Mechanisms in $Sr_{1-x}Ba_xTiO_3$ Solid Solution at Low Doping Concentration*, Mater. Res. Bull. **36**, 1693 (2001).

[31] V. V. Lemanov, E. P. Smirnova, and E. A. Tarakanov, *Ferroelectric Properties of $SrTiO_3$-$PbTiO_3$ Solid Solutions*, Phys. Solid State **39**, 628 (1997).

[32] A. Durán, E. Martínez, J. A. Díaz, and J. M. Siqueiros, *Ferroelectricity at Room Temperature in Pr-Doped $SrTiO_3$*, J. Appl. Phys. **97**, 104109 (2005).

[33] W. J. Burke and R. J. Pressley, *Stress Induced Ferroelectricity in $SrTiO_3$*, Solid State Commun. **9**, 191 (1971).

[34] H. Uwe and T. Sakudo, *Stress-Induced Ferroelectricity and Soft Phonon Modes in $SrTiO_3$*, Phys. Rev. B **13**, 271 (1976).

[35] J. H. Haeni, P. Irvin, W. Chang, R. Uecker, P. Reiche, Y. L. Li, S. Choudhury, W. Tian, M. E. Hawley, B. Craigo, A. K. Tagantsev, X. Q. Pan, S. K. Streiffer, L. Q. Chen, S. W. Kirchoefer, J. Levy, and D. G. Schlom, *Room-Temperature Ferroelectricity in Strained $SrTiO_3$*, Nature **430**, 758 (2004).

[36] R. Russell, N. Ratcliff, K. Ahadi, L. Dong, S. Stemmer, and J. W. Harter, *Ferroelectric Enhancement of Superconductivity in Compressively Strained $SrTiO_3$ Films*, Phys. Rev. Mater. **3**, 091401(R) (2019).

[37] Z. Tan, Y. Peng, J. An, Q. Zhang, and J. Zhu, *Critical Role of Order-Disorder Behavior in Perovskite Ferroelectric $KNbO_3$*, Inorg. Chem. **60**, 7961 (2021).

[38] Y. Yamada and G. Shirane, *Neutron Scattering and Nature of the Soft Optical Phonon in $SrTiO_3$*, J. Phys. Soc. Jpn. **26**, 396 (1969).

[39] S. Salmani-Rezaie, K. Ahadi, W. M. Strickland, and S. Stemmer, *Order-Disorder Ferroelectric Transition of Strained $SrTiO_3$*, Phys. Rev. Lett. **125**, 087601 (2020).

[40] A. Verma, S. Raghavan, S. Stemmer, and D. Jena, *Ferroelectric Transition in Compressively Strained $SrTiO_3$ Thin Films*, Appl. Phys. Lett. **107**, 192908 (2015).

[41] L. P. Gor'kov, *Phonon Mechanism in the Most Dilute Superconductor N-Type $SrTiO_3$*, Proc. Natl. Acad. Sci. U. S. A. **113**, 4646 (2016).

[42] L. V. Gurevich, A. I. Larkin, and Y. A. Firsov, *Possibility of Superconductivity in Semiconductors*, Sov. Phys. Sol. State **4**, 131 (1962).

[43] L. P. Gor'kov, *Back to Mechanisms of Superconductivity in Low-Doped Strontium Titanate*, J. Supercond. Nov. Magn. **30**, 845 (2017).

[44] A. Stucky, G. W. Scheerer, Z. Ren, D. Jaccard, J. M. Poumirol, C. Barreteau, E. Giannini, and D. Van Der Marel, *Isotope Effect in Superconducting N-Doped $SrTiO_3$*, Sci. Rep. **6**, 37582 (2016).

[45] C. W. Rischau, X. Lin, C. P. Grams, D. Finck, S. Harms, J. Engelmayer, T. Lorenz, Y. Gallais, B. Fauqué, J. Hemberger, and K. Behnia, *A Ferroelectric Quantum Phase Transition inside the Superconducting Dome of $Sr_{1-x}Ca_xTiO_{3-\delta}$*, Nat. Phys. **13**, 643 (2017).

[46] T. Moriya, *Developments of the Theory of Spin Fluctuations and Spin Fluctuation-Induced Superconductivity*, Proc. Japan Acad. Ser. B: Phys. Biol. Sci. **82**, 1 (2006).

[47] J. M. Edge, Y. Kedem, U. Aschauer, N. A. Spaldin, and A. V. Balatsky, *Quantum Critical Origin of the Superconducting Dome in $SrTiO_3$*, Phys. Rev. Lett. **115**, 247002 (2015).

[48] M. Gabay and J. Triscone, *Superconductivity: Ferroelectricity Woos Pairing*, Nat.

Phys. **13**, 624 (2017).

[49] Y. Tomioka, N. Shirakawa, and I. H. Inoue, *Superconductivity Enhanced in the Polar Metal Region of $Sr_{0.95}Ba_{0.05}TiO_3$ and $Sr_{0.985}Ca_{0.015}TiO_3$ Revealed by the Systematic Nb Doping*, arXiv:2203.16208 (2022).

[50] X. Lin, G. Bridoux, A. Gourgout, G. Seyfarth, S. Krämer, M. Nardone, B. Fauqué, and K. Behnia, *Critical Doping for the Onset of a Two-Band Superconducting Ground State in $SrTiO_{3-\delta}$*, Phys. Rev. Lett. **112**, 207002 (2014).

[51] G. Binnig, A. Baratoff, H. E. Hoenig, and J. G. Bednorz, *Two-Band Superconductivity in Nb-Doped $SrTiO_3$*, Phys. Rev. Lett. **45**, 1352 (1980).

[52] J. M. Edge and A. V. Balatsky, *Upper Critical Field as a Probe for Multiband Superconductivity in Bulk and Interfacial STO*, J. Supercond. Nov. Magn. **28**, 2373 (2015).

[53] S. Salmani-Rezaie, L. Galletti, T. Schumann, and R. Russell, *Superconductivity in Magnetically Doped $SrTiO_3$*, Appl. Phys. Lett. **118**, 202602 (2021).

[54] V. Kozii and L. Fu, *Odd-Parity Superconductivity in the Vicinity of Inversion Symmetry Breaking in Spin-Orbit-Coupled Systems*, Phys. Rev. Lett. **115**, 207002 (2015).

[55] S. Kanasugi and Y. Yanase, *Spin-Orbit-Coupled Ferroelectric Superconductivity*, Phys. Rev. B **98**, 024521 (2018).

[56] S. Kanasugi and Y. Yanase, *Multiorbital Ferroelectric Superconductivity in Doped $SrTiO_3$*, Phys. Rev. B **100**, 094504 (2019).

[57] T. Schumann, L. Galletti, H. Jeong, K. Ahadi, W. M. Strickland, S. Salmani-Rezaie, and S. Stemmer, *Possible Signatures of Mixed-Parity Superconductivity in Doped*

Polar $SrTiO_3$ Films, Phys. Rev. B **101**, 100503(R) (2020).

[58] H. Jeong, N. G. Combs, S. Munyan, A. Rashidi, and S. Stemmer, *Reducing Surface Depletion of Superconducting $SrTiO_3$ Films with $EuTiO_3$ Capping Layers*, Appl. Phys. Lett. **119**, 162601 (2021).

[59] H. Jeong, R. Russell, N. G. Combs, T. N. Pardue, J. W. Harter, and S. Stemmer, *Similarity in the Critical Thicknesses for Superconductivity and Ferroelectricity in Strained $SrTiO_3$ Films*, Appl. Phys. Lett. **121**, 012601 (2022).

[60] J. J. Cuomo, D. L. Pappas, J. Bruley, J. P. Doyle, and K. L. Saenger, *Vapor Deposition Processes for Amorphous Carbon Films with sp^3 Fractions Approaching Diamond*, J. Appl. Phys. **70**, 1706 (1991).

[61] A. Y. Cho and J. R. Arthur, *Molecular Beam Epitaxy*, Prog. Solid State Chem. **10**, 157 (1975).

[62] H. Asahi and Y. Horikoshi, *Molecular Beam Epitaxy: Materials and Applications for Electronics and Optoelectronics* (John Wiley & Sons, 2019).

[63] A. Prakash, P. Xu, X. Wu, G. Haugstad, X. Wang, and B. Jalan, *Adsorption-Controlled Growth and the Influence of Stoichiometry on Electronic Transport in Hybrid Molecular Beam Epitaxy-Grown $BaSnO_3$ Films*, J. Mater. Chem. C **5**, 5730 (2017).

[64] C. D. Theis, J. Yeh, D. G. Schlom, M. E. Hawley, and G. W. Brown, *Adsorption-Controlled Growth of $PbTiO_3$ by Reactive Molecular Beam Epitaxy*, Thin Solid Films **325**, 107 (1998).

[65] B. Jalan, P. Moetakef, and S. Stemmer, *Molecular Beam Epitaxy of $SrTiO_3$ with a Growth Window*, Appl. Phys. Lett. **95**, 032906 (2009).

[66] C. R. Freeze, *Molecular Beam Epitaxy of Wide-Band Gap Perovskiteoxides: (Ba, Sr)TiO_3 and $BaSnO_3$*, UC Santa Barbara, Santa Barbara, Ph.D. dissertation (2019).

[67] B. Jalan, R. Engel-Herbert, N. J. Wright, and S. Stemmer, *Growth of High-Quality $SrTiO_3$ Films Using a Hybrid Molecular Beam Epitaxy Approach*, J. Vac. Sci. Technol. A **27**, 461 (2009).

[68] B. Jalan, J. Cagnon, T. E. Mates, and S. Stemmer, *Analysis of Carbon in $SrTiO_3$ Grown by Hybrid Molecular Beam Epitaxy*, J. Vac. Sci. Technol. A **27**, 1365 (2009).

[69] R. C. Haislmaier, R. Engel-Herbert, and V. Gopalan, *Stoichiometry as Key to Ferroelectricity in Compressively Strained $SrTiO_3$ Films*, Appl. Phys. Lett. **109**, 032901 (2016).

[70] S. Hasegawa, *Reflection High-Energy Electron Diffraction*, John Wiley & Sons, Inc., Hoboken, NJ, USA, (2002)

[71] A. P. Kajdos and S. Stemmer, *Surface Reconstructions in Molecular Beam Epitaxy of $SrTiO_3$*, Appl. Phys. Lett. **105**, 191901 (2014).

[72] J. Lapano, M. Brahlek, L. Zhang, J. Roth, A. Pogrebnyakov, and R. Engel-Herbert, *Scaling Growth Rates for Perovskite Oxide Virtual Substrates on Silicon*, Nat. Commun. **10**, 2464 (2019).

[73] J. H. van der Merwe, *Misfit Dislocation Generation in Epitaxial Layers*, Crit. Rev. Solid State Mater. Sci. **17**, 187 (1991).

[74] J. H. van der Merwe, *Strain Relaxation in Epitaxial Overlayers*, J. Electron. Mater. **20**, 793 (1991).

[75] L. J. van der Pauw, *A Method of Measuring Specific Resistivity and Hall Effect of Discs of Arbitrary Shapes*, Philips Res. Rep. **13**, 1 (1958).

[76] NIST, *The Hall Effect*, (2022, July 19), Available: https://www.nist.gov/pml/nanoscale-device-characterization-division/popular-links/hall-effect/hall-effect

[77] M. Biderang, H. Yavari, M. H. Zare, P. Thalmeier, and A. Akbari, *Edge Currents as a Probe of the Strongly Spin-Polarized Topological Noncentrosymmetric Superconductors*, Phys. Rev. B **98**, 014524 (2018).

[78] C. Nayak, S. H. Simon, A. Stern, M. Freedman, and S. Das Sarma, *Non-Abelian Anyons and Topological Quantum Computation*, Rev. Mod. Phys. **80**, 1083 (2008).

[79] G. L. J. A. Rikken and E. Raupach, *Observation of Magneto-Chiral Dichroism*, Nature **390**, 493 (1997).

[80] R. Wakatsuki, Y. Saito, S. Hoshino, Y. M. Itahashi, T. Ideue, M. Ezawa, Y. Iwasa, and N. Nagaosa, *Nonreciprocal Charge Transport in Noncentrosymmetric Superconductors*, Sci. Adv. **3**, e1602390 (2017).

[81] T. Wang, K. Ganguly, P. Marshall, P. Xu, and B. Jalan, *Critical Thickness and Strain Relaxation in Molecular Beam Epitaxy-Grown $SrTiO_3$ Films*, Appl. Phys. Lett. **103**, 212904 (2013).

[82] A. Ohtomo and H. Y. Hwang, *Surface Depletion in Doped $SrTiO_3$ Thin Films*, Appl. Phys. Lett. **84**, 1716 (2004).

[83] M. Kim, Y. Kozuka, C. Bell, Y. Hikita, and H. Y. Hwang, *Intrinsic Spin-Orbit Coupling in Superconducting δ-Doped $SrTiO_3$ Heterostructures*, Phys. Rev. B **86**, 085121 (2012).

[84] A. M. Clogston, *Upper Limit for the Critical Field in Hard Superconductors*, Phys. Rev. Lett. **9**, 266 (1962).

[85] A. M. Toxen, *Critical Fields of Thin Superconducting Films. I. Thickness Effects*, Phys. Rev. **127**, 382 (1962).

[86] G. Rickayzen, *Critical Magnetic Field of a Thin Film of Superconductor*, Phys. Rev. **138**, A73 (1965).

[87] M. Smidman, M. B. Salamon, H. Q. Yuan, and D. F. Agterberg, *Superconductivity and Spin-Orbit Coupling in Non-Centrosymmetric Materials: A Review*, Rep. Prog. Phys. **80**, 036501 (2017).

[88] R. Wakatsuki and N. Nagaosa, *Nonreciprocal Current in Noncentrosymmetric Rashba Superconductors*, Phys. Rev. Lett. **121**, 026601 (2018).

[89] D. Choe, M. J. Jin, S. I. Kim, H. J. Choi, J. Jo, I. Oh, J. Park, H. Jin, H. C. Koo, B. C. Min, S. Hong, H. W. Lee, S. H. Baek, and J. W. Yoo, *Gate-Tunable Giant Nonreciprocal Charge Transport in Noncentrosymmetric Oxide Interfaces*, Nat. Commun. **10**, 4510 (2019).

[90] T. Ideue, S. Koshikawa, H. Namiki, T. Sasagawa, and Y. Iwasa, *Giant Nonreciprocal Magnetotransport in Bulk Trigonal Superconductor $PbTaSe_2$*, Phys. Rev. Res. **2**, 042046(R) (2020).

[91] Y. M. Itahashi, T. Ideue, Y. Saito, S. Shimizu, T. Ouchi, T. Nojima, and Y. Iwasa, *Nonreciprocal Transport in Gate-Induced Polar Superconductor $SrTiO_3$*, Sci. Adv. **6**, eaay9120 (2020).

[92] Y. Aiura, I. Hase, H. Bando, T. Yasue, T. Saitoh, and D. S. Dessau, *Photoemission Study of the Metallic State of Lightly Electron-Doped $SrTiO_3$*, Surf. Sci. **515**, 61 (2002).

[93] T. Hara, T. Ishiguro, and K. Shinozaki, *Ultraviolet-Light-Induced Desorption of*

Oxygen from $SrTiO_3$ Surfaces, Jpn. J. Appl. Phys. **50**, 041502 (2011).

[94] W. Meevasana, P. D. C. King, R. H. He, S. K. Mo, M. Hashimoto, A. Tamai, P. Songsiriritthigul, F. Baumberger, and Z. X. Shen, *Creation and Control of a Two-Dimensional Electron Liquid at the Bare $SrTiO_3$ Surface*, Nat. Mater. **10**, 114 (2011).

[95] T. A. Cain, A. P. Kajdos, and S. Stemmer, *La-doped $SrTiO_3$ Films with Large Cryogenic Thermoelectric Power Factors*, Appl. Phys. Lett. **102**, 182101 (2013).

[96] S. J. Allen, B. Jalan, S. Lee, D. G. Ouellette, G. Khalsa, J. Jaroszynski, S. Stemmer, and A. H. Macdonald, *Conduction-Band Edge and Shubnikov-de Haas Effect in Low-Electron-Density $SrTiO_3$*, Phys. Rev. B **88**, 045114 (2013).

[97] Y. Kozuka, Y. Hikita, C. Bell, and H. Y. Hwang, *Dramatic Mobility Enhancements in Doped $SrTiO_3$ Thin Films by Defect Management*, Appl. Phys. Lett. **97**, 012107 (2010).

[98] J. Köhler, R. Dinnebier, and A. Bussmann-Holder, *Structural Instability of $EuTiO_3$ from X-Ray Powder Diffraction*, Phase Transitions **85**, 949 (2012).

[99] T. R. McGuire, M. W. Shafer, R. J. Joenk, H. A. Alperin, and S. J. Pickart, *Magnetic Structure of $EuTiO_3$*, J. Appl. Phys. **37**, 981 (1966).

[100] T. Katsufuji and H. Takagi, *Coupling between Magnetism and Dielectric Properties in Quantum Paraelectric $EuTiO_3$*, Phys. Rev. B **64**, 054415 (2001).

[101] A. Ohtomo and H. Y. Hwang, *A High-Mobility Electron Gas at the $LaAlO_3/SrTiO_3$ Heterointerface*, Nature **427**, 423 (2004).

[102] P. Moetakef, T. A. Cain, D. G. Ouellette, J. Y. Zhang, D. O. Klenov, A. Janotti, C. G. Van De Walle, S. Rajan, S. J. Allen, and S. Stemmer, *Electrostatic Carrier Doping of $GdTiO_3/SrTiO_3$ Interfaces*, Appl. Phys. Lett. **99**, 232116 (2011).

[103] K. S. Takahashi, H. Ishizuka, T. Murata, Q. Y. Wang, Y. Tokura, N. Nagaosa, and M. Kawasaki, *Anomalous Hall Effect Derived from Multiple Weyl Nodes in High-Mobility $EuTiO_3$ Films*, Sci. Adv. **4**, eaar7880 (2018).

[104] K. Ahadi, L. Galletti, and S. Stemmer, *Evidence of a Topological Hall Effect in $Eu_{1-x}Sm_xTiO_3$*, Appl. Phys. Lett. **111**, 172403 (2017).

[105] T. Katsufuji and Y. Tokura, *Transport and Magnetic Properties of a Ferromagnetic Metal: $Eu_{1-x}R_xTiO_3$*, Phys. Rev. B **60**, R15021(R) (1999).

[106] O. F. Shoron, S. Raghavan, C. R. Freeze, and S. Stemmer, *$BaTiO_3/SrTiO_3$ Heterostructures for Ferroelectric Field Effect Transistors*, Appl. Phys. Lett. **110**, 232902 (2017).

[107] E. Mikheev, C. R. Freeze, B. J. Isaac, T. A. Cain, and S. Stemmer, *Separation of Transport Lifetimes in $SrTiO_3$-Based Two-Dimensional Electron Liquids*, Phys. Rev. B **91**, 165125 (2015).

[108] T. Holstein, *Hall effect in impurity conduction*, Phys. Rev. **124**, 1329–1347 (1961)

[109] Z. Porter, R. F. Need, K. Ahadi, Y. Zhao, Z. Xu, B. J. Kirby, J. W. Lynn, S. Stemmer, and S. D. Wilson, *Correlating Magnetic Structure and Magnetotransport in Semimetal Thin Films of $Eu_{1-X}Sm_xTiO_3$*, Phys. Rev. Mater. **4**, 054411 (2020).

[110] N. R. Werthamer, *Theory of the Superconducting Transition Temperature and Energy Gap Function of Superposed Metal Films*, Phys. Rev. **132**, 2440 (1963).

[111] P. G. De Gennes and E. Guyon, *Superconductivity in normal metals*, Phys. Lett. **3**, 168-169 (1963).

[112] L. Bjaalie, B. Himmetoglu, L. Weston, A. Janotti, and C. G. Van De Walle, *Oxide Interfaces for Novel Electronic Applications*, New J. Phys. **16**, 025005 (2014).

[113] Z. Gui and A. Janotti, *Carrier-Density-Induced Ferromagnetism in $EuTiO_3$ Bulk and Heterostructures*, Phys. Rev. Lett. **123**, 127201 (2019).

[114] S. Salmani-Rezaie, H. Jeong, R. Russell, J. W. Harter, and S. Stemmer, *Role of Locally Polar Regions in the Superconductivity of $SrTiO_3$*, Phys. Rev. Mater. **5**, 104801 (2021).

[115] Y. Tomioka, N. Shirakawa, K. Shibuya, and I. H. Inoue, *Enhanced Superconductivity Close to a Non-Magnetic Quantum Critical Point in Electron-Doped Strontium Titanate*, Nat. Commun. **10**, 738 (2019).

[116] V. M. Edel'shtein, *Characteristics of the Cooper Pairing in Two-Dimensional Noncentrosymmetric Electron Systems*, Sov. Phys. JETP **68**, 1244-1249 (1989); available at http://www.jetp.ras.ru/cgi-bin/dn/e_068_06_1244.pdf.

[117] V. M. Edelstein, *Magnetoelectric Effect in Polar Superconductors*, Phys. Rev. Lett. **75**, 2004-2007 (1995).

[118] Y. Tokura and N. Nagaosa, *Nonreciprocal Responses from Non-Centrosymmetric Quantum Materials*, Nat. Commun. **9**, 3740 (2018).

[119] Y. Kedem, *Novel Pairing Mechanism for Superconductivity at a Vanishing Level of Doping Driven by Critical Ferroelectric Modes*, Phys. Rev. B **98**, 220505(R) (2018).

[120] C. Enderlein, J. F. de Oliveira, D. A. Tompsett, E. B. Saitovitch, S. S. Saxena, G. G. Lonzarich, and S. E. Rowley, *Superconductivity Mediated by Polar Modes in Ferroelectric Metals*, Nat. Commun. **11**, 4852 (2020).

[121] M. N. Gastiasoro, T. V. Trevisan, and R. M. Fernandes, *Anisotropic Superconductivity Mediated by Ferroelectric Fluctuations in Cubic Systems with Spin-Orbit Coupling*, Phys. Rev. B **101**, 174501 (2020).

[122] C. W. Rischau, D. Pulmannová, G. W. Scheerer, A. Stucky, E. Giannini, and D. van der Marel, *Isotope Tuning of the Superconducting Dome of Strontium Titanate*, Phys. Rev. Res. **4**, 013019 (2022).

[123] T. Tybell, C. H. Ahn, and J. M. Triscone, *Ferroelectricity in Thin Perovskite Films*, Appl. Phys. Lett. **75**, 856 (1999).

[124] D. D. Fong, G. B. Stephenson, S. K. Streiffer, J. A. Eastman, O. Aucielo, P. H. Fuoss, and C. Thompson, *Ferroelectricity in Ultrathin Perovskite Films*, Science **304**, 1650 (2004).

[125] J. Junquera and P. Ghosez, *Critical Thickness for Ferroelectricity in Perovskite Ultrathin Films*, Nature **422**, 506 (2003).

[126] D. J. Kim, J. Y. Jo, Y. S. Kim, Y. J. Chang, J. S. Lee, J. G. Yoon, T. K. Song, and T. W. Noh, *Polarization Relaxation Induced by a Depolarization Field in Ultrathin Ferroelectric $BaTiO_3$ Capacitors*, Phys. Rev. Lett. **95**, 237602 (2005).

[127] D. B. Haviland, Y. Liu, and A. M. Goldman, *Onset of Superconductivity in the Two-Dimensional Limit*, Phys. Rev. Lett. **62**, 2180 (1989).

[128] N. Pertsev, A. Tagantsev, and N. Setter, *Phase Transitions and Strain-induced Ferroelectricity in Epitaxial Thin Films*, Phys. Rev. B **61**, R825(R) (2000).

[129] W. Zhong, R. D. King-Smith, and D. Vanderbilt, *Giant LO-TO Splittings in Perovskite Ferroelectrics*, Phys. Rev. Lett. **72**, 3618 (1994).

[130] R. C. Haislmaier, R. Engel-Herbert, and V. Gopalan, *Stoichiometry as Key to Ferroelectricity in Compressively Strained $SrTiO_3$ Films*, Appl. Phys. Lett. **109**, 032901 (2016).

[131] N. Reyren, S. Thiel, A. D. Caviglia, L. F. Kourkoutis, G. Hammerl, C. Richter, C. W.

Schneider, T. Kopp, A. S. Ruetschi, D. Jaccard, M. Gabay, D. A. Muller, J. M. Triscone, and J. Mannhart, *Superconducting Interfaces Between Insulating Oxides*, Science **317**, 1196 (2007).

[132] Y. Kozuka, M. Kim, C. Bell, B. G. Kim, Y. Hikita, and H. Y. Hwang, *Two-Dimensional Normal-State Quantum Oscillations in a Superconducting Heterostructure*, Nature **462**, 487 (2009).

[133] Y. Liu, K. A. McGreer, B. Nease, D. B. Haviland, G. Martinez, J. W. Halley, and A. M. Goldman, *Scaling of the Insulator-to-Superconductor Transition in Ultrathin Amorphous Bi Films*, Phys. Rev. Lett. **67**, 2068 (1991).

[134] A. D. Caviglia, M. Gabay, S. Gariglio, N. Reyren, C. Cancellieri, and J. M. Triscone, *Tunable Rashba Spin-Orbit Interaction at Oxide Interfaces*, Phys. Rev. Lett. **104**, 126803 (2010).

[135] Y. L. Li, S. Choudhury, J. H. Haeni, M. D. Biegalski, A. Vasudevarao, A. Sharan, H. Z. Ma, J. Levy, V. Gopalan, S. Trolier-Mckinstry, D. G. Schlom, Q. X. Jia, and L. Q. Chen, *Phase Transitions and Domain Structures in Strained Pseudocubic (100) SrTi O_3 Thin Films*, Phys. Rev. B **73**, 184112 (2006).

[136] M. D. Biegalski, D. D. Fong, J. A. Eastman, P. H. Fuoss, S. K. Streiffer, T. Heeg, J. Schubert, W. Tian, C. T. Nelson, X. Q. Pan, M. E. Hawley, M. Bernhagen, P. Reiche, R. Uecker, S. Trolier-Mckinstry, and D. G. Schlom, *Critical Thickness of High Structural Quality $SrTiO_3$ Films Grown on Orthorhombic (101) $DyScO_3$*, J. Appl. Phys. **104**, 114109 (2008).

[137] F. Ando, Y. Miyasaka, T. Li, J. Ishizuka, T. Arakawa, Y. Shiota, T. Moriyama, Y. Yanase, and T. Ono, *Observation of Superconducting Diode Effect*, Nature **584**, 373

(2020).

[138] Z. Porter, R. F. Need, K. Ahadi, Y. Zhao, Z. Xu, B. J. Kirby, J. W. Lynn, S. Stemmer, and S. D. Wilson, *Correlating Magnetic Structure and Magnetotransport in Semimetal Thin Films of* $Eu_{1-x}Sm_xTiO_3$, Phys. Rev. Mater. **4**, 054411 (2020).

[139] H. Wu, Y. Wang, Y. Xu, P. K. Sivakumar, C. Pasco, U. Filippozzi, S. S. P. Parkin, Y. J. Zeng, T. McQueen, and M. N. Ali, *The Field-Free Josephson Diode in a van Der Waals Heterostructure*, Nature **604**, 653 (2022).

[140] H. Narita, J. Ishizuka, R. Kawarazaki, and D. Kan, *Field-Free Superconducting Diode Effect in Noncentrosymmetric Superconductor/Ferromagnet Multilayers*, Nat. Nanotechnol. (2022). https://doi.org/10.1038/s41565-022-01159-4